Parametrical study on separation-induced transition and vortex dynamics of a reversed pitching airfoil

Lei Shi [a,b], Yefang Wang [a], Desheng Zhang [a,*], Annie-Claude Bayeul-Lainé [b], Olivier Coutier-Delgosha [b,c]

[a] *Research Center of Fluid Machinery Engineering and Technology, Jiangsu University, Zhenjiang 212013, China*
[b] *Arts et Métiers ParisTech, ONERA, CNRS, Univ. Lille, Centrale Lille, UMR 9014-LMFL-Laboratoire de Mécanique des Fluides de Lille-Kampé de Fériet, F-59000 Lille, France*
[c] *Kevin T. Crofton Department of Aerospace and Ocean Engineering, Virginia Tech, Blacksburg, Virginia 24060, USA*

ABSTRACT

The pitching airfoils, applied to the vertical axis turbines and propellers, are critical to extract more energy from the environment. At retreating side, when the airfoil blunt leading edge becomes the trailing edge, the transition and vortex dynamics are quite different from that at advancing side. The goal of the present work is to investigate the transition and vortex evolution over the reversed pitching airfoil, with main focus on the parametrical effect, including the mean pitching angle and pitching amplitude, reduced frequency and Reynolds number. The main results show that the flow structure on the reversed airfoil is more complex compared with that over the forward airfoil due to the earlier flow separation near the sharp leading edge. Then, the transition on the reversed airfoil firstly occurs within the separated shear layer near the sharp leading edge, and then the flow reattaches, leading to the generation of the leading-edge vortex. Near the blunt trailing edge, the second transition appears on two sides, resulting in the asymmetrical boundary layer as the incidence increases continuously. This event is totally different from that on the forward airfoil, shown by the transition always moving from the trailing edge to the leading edge. The flow unsteadiness of the reversed airfoil is mainly induced by the separated shear layer and leading-edge vortex, which is greatly affected by different parameters. Besides, the trajectory of some specific vortices also depends on the working conditions significantly. It is believed that this work can deepen the understandings of underlying flow physics of the reversed airfoils.

1. Introduction

As the basic elements, the oscillating airfoils/hydrofoils with different kinematics are extensively used in many engineering applications, such as the vertical axis wind turbine (VAWT), underwater propulsion system and micro air vehicle (MAV). The flow structures are always complex as the airfoil experiences a large variation of incidences, even for the pure pitching motion. In the process of the oscillation, one of the noticeable events is the laminar-turbulence transition induced by the laminar separation bubble (LSB) attached on the suction side, thanks to the existence of the strong adverse pressure gradient. The laminar boundary layer is extremely sensitive to the disturbance from the external environment and then separates. After that, the reattachment of the energetic separated shear layer results in the formation of the separation bubble, which is the main source for the occurrence of the transition. Nowadays, the transition effect has been attracting more and more attention to many large-scale aerial and submarine devices with complicated configurations, such as the stratospheric airship (Shen et al., 2015), Airlander 50 (Carri ó n et al., 2016) and autonomous underwater vehicles (AUV) (Salari and Rava, 2017). Sometimes, if there is a little flow separation on the surface, the skin friction drag is also critical to the prediction of the drag. In other words, the length of the laminar flow region has substantial effect on the performance, which is determined by the transition location. Actually, the transition is affected by many important parameters, including the Reynolds number (Kim and Chang, 2014), airfoil geometry and elasticity (Chao et al., 2018; Dai et al., 2012), inflow turbulence intensity (Kim and Xie, 2016) and surface roughness (Huebsch and Rothmayer, 2002). The presence of LSB can lead to some undesirable consequences, such as the performance degradation, noise and vibration and abrupt stall.

---

* Corresponding author.
  E-mail address: zds@ujs.edu.cn (D. Zhang).

(a) Global mesh

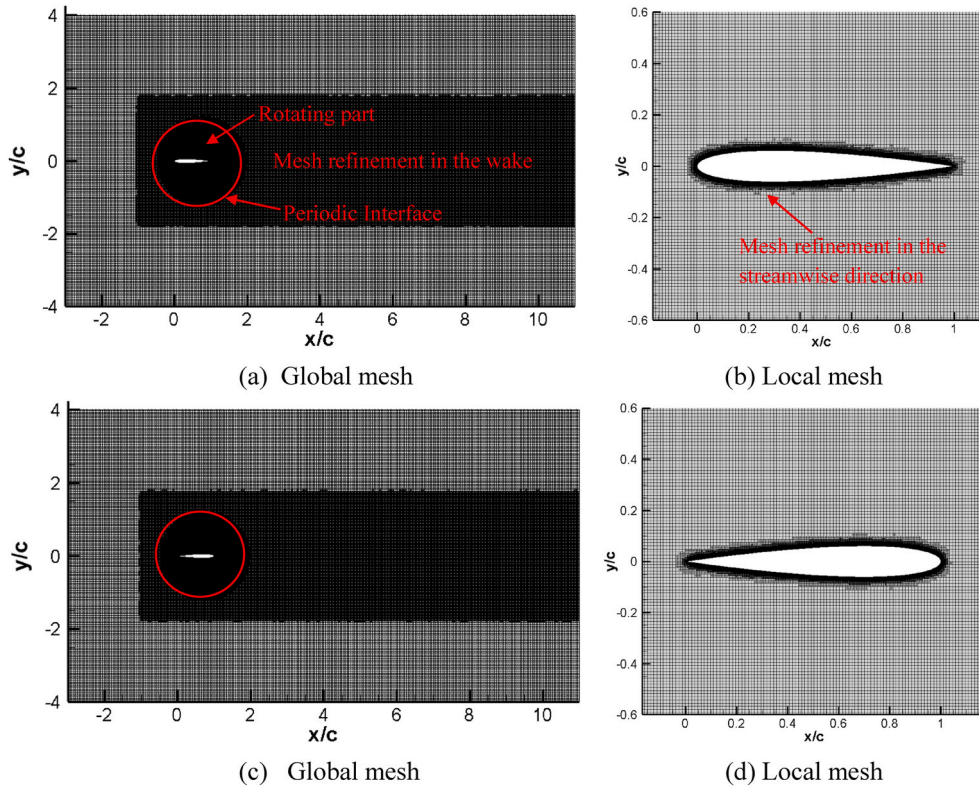(b) Local mesh

(c) Global mesh

(d) Local mesh

Fig. 1. Mesh generation in the computational domain and near the airfoil surface.

Table 1
The mesh distribution for the reversed pitching airfoil.

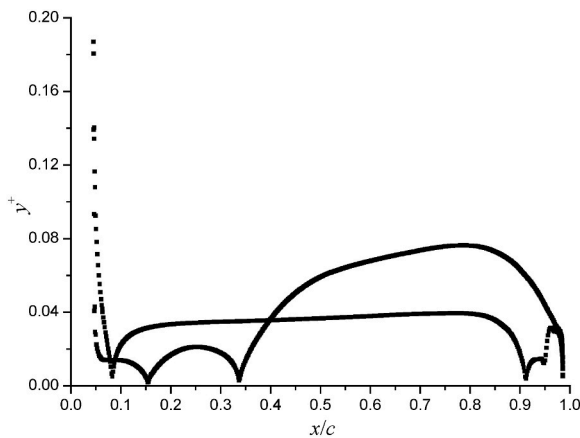|	Total mesh nodes	Target size of the mesh near the surface (m)	Prism layer thickness (m)	Number of layers	Maximal y^+
Mesh 1	159,794	5×10^{-4}	2.0×10^{-3}	50	0.24
Mesh 2	209,598	4×10^{-4}	2.5×10^{-3}	70	0.17
Mesh 3	248,069	3×10^{-4}	3.0×10^{-3}	80	0.10

Fig. 2. Distribution of y^+ on the reversed airfoil surface at maximal pitching incidence.

For the moment, there are two main numerical approaches that can be applied to model the onset of the transition: one is the turbulence model based on the Reynolds Averaged Navier-Stokes (RANS) method

coupled with the transition model and the other one is the large eddy simulation (LES). Indeed, the LES is capable of obtaining detailed and reliable information about the flow quantities of the global flow field, but it is still unfeasible due to the high requirements of the computational resources. The study on the dynamic stall of pitching airfoils using the LES methodology can refer to the related references (Visbal and Garmann, 2018; Guillaud et al., 2018; Rahromostaqim et al., 2016). For most engineering flows, the RANS-based turbulence models are still the primary tools, which can gain the acceptable results in aspects of the main vortex structures and some mean turbulence variables. Many previous investigations have been conducted for the oscillating airfoils and the main emphasis is on the mechanism of the dynamic stall. For some specific examples, Wang et al., 2010, 2012 compared the effect of various turbulence models on the dynamic stall of a pitching airfoil and the parameters consisting of the reduced frequency, mean pitching incidence and pitching amplitude are considered. It concludes that the SST (shear stress transport) k-ω (turbulent kinetic energy-specific dissipation rate) model (Menter et al., 2003) can capture well the vortex-shedding predominated flow structures only for the relative high incidence. But for the high incidences representing the stall and deep-stall conditions, the SST k-ω model based on the detached eddy simulation (DES) approach (Nichols, 2006) is recommended because of the superiority in resolving the vortex-dominated flows. Then, Tseng et al. (Tseng and Hu, 2016; Tseng and Cheng, 2015) revealed the originality of various vortex structures and the mechanism of the delayed stall associated with the leading-edge vortex (LEV) for a pitching airfoil using the SST k-ω model and a new Lagrangian coherent structure. Furthermore, Ducoin et al. (2009) used the SST $\gamma - \overline{Re_{\theta t}}$ (intermittency-transition momentum thickness Reynolds number) model (Menter et al., 2006a, 2006b) to simulate the near-wall transitional flow around a pitching hydrofoil with the incidences ranging from $0°$ to $15°$ and it is observed that the calculated wall pressure shows a good agreement with the experiments as well as the transition location. In addition, Karbasian and Kim (2016) and Singh and Páscoa (Singh and P
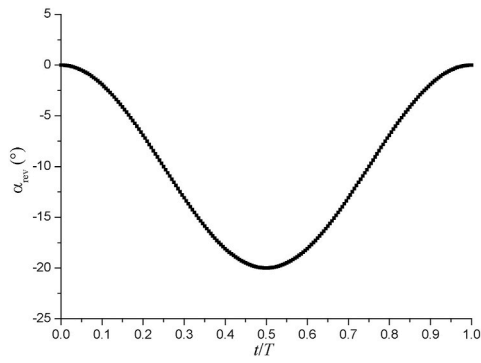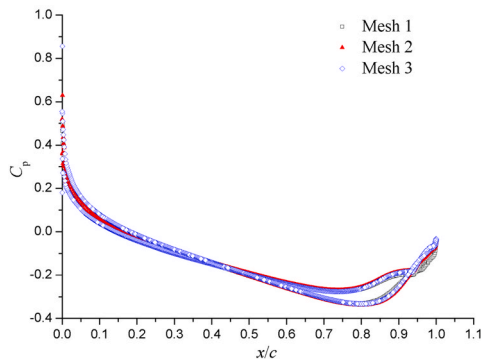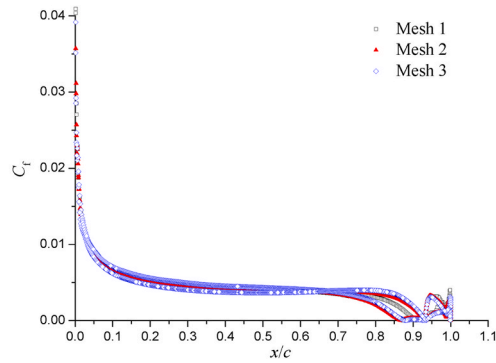
(a) Pitching kinematic
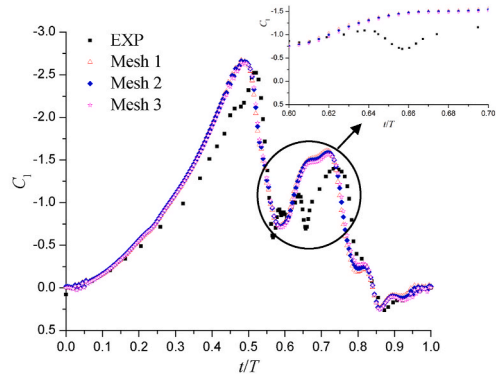
(b) Instantaneous lift coefficient

Fig. 3. Pitching kinematic and instantaneous lift coefficient in a revolution.

(a) Pressure coefficient

(b) Skin friction coefficient

Fig. 4. Pressure and skin friction coefficients for different meshes.

Table 2
Order of the accuracy for the time-averaged lift coefficient.

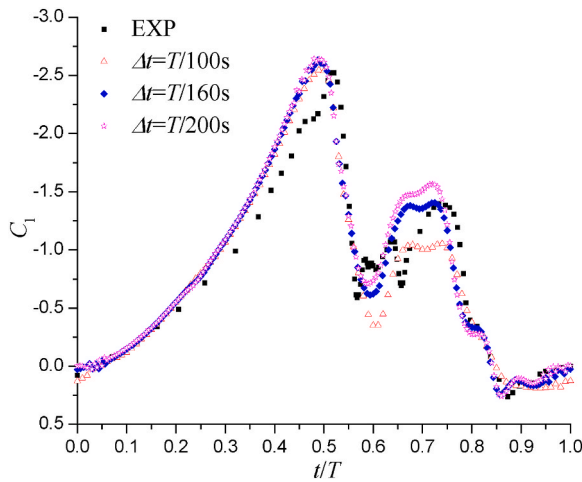|	f_1	f_2	f_3	ε_{21}	ε_{32}	R	p_{21}/p_{32}	GCI$_{21}$ (%)	GCI$_{32}$ (%)
C_L	−0.865	−0.860	−0.859	0.00512	0.00132	0.258	9.99/16.1	0.257	0.0667

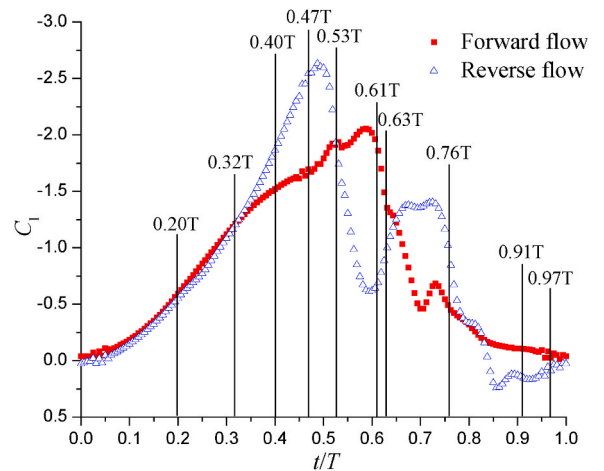**Fig. 5.** Effect of the time-step on instantaneous lift coefficient in a revolution.

Fig. 6. Instantaneous lift coefficient variation of forward and reversed airfoils in a revolution.
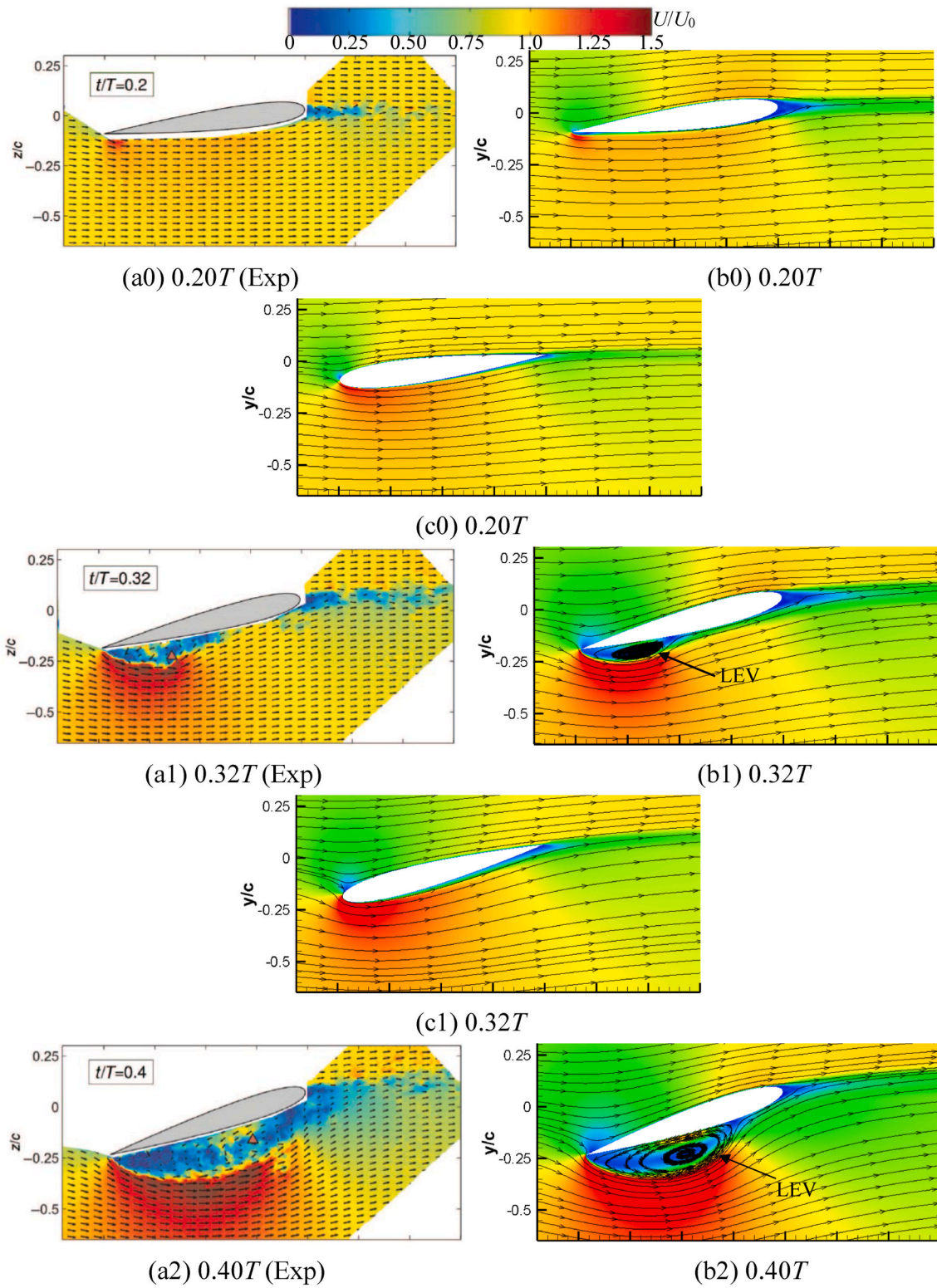
Fig. 7. Evolution of flow structures over forward and reversed airfoils in a revolution.

á scoa, 2019) also showed that the SST $\gamma - \overline{Re_{\theta t}}$ transition model has the capability in predicting the global performance and vortical flows when the incidence is smaller than $20°$. For the more complicated two-phase flow, Huang et al. (2013) employed the SST $\gamma - \overline{Re_{\theta t}}$ transition model along with a homogeneous cavitation model to calculate the unsteady cavitating flows around a pitching hydrofoil. The main conclusion is that

the pitching rate can cause the more intensive cavitation and change the cavity shedding frequency significantly, as well as the local vorticity filed as a consequence of the periodic evolution of sheet/cloud cavities. Moreover, the choice of the turbulence model with the consideration of the transition is also of great importance to the prediction of the performance and flow structures of vertical-axis turbines and propellers. In

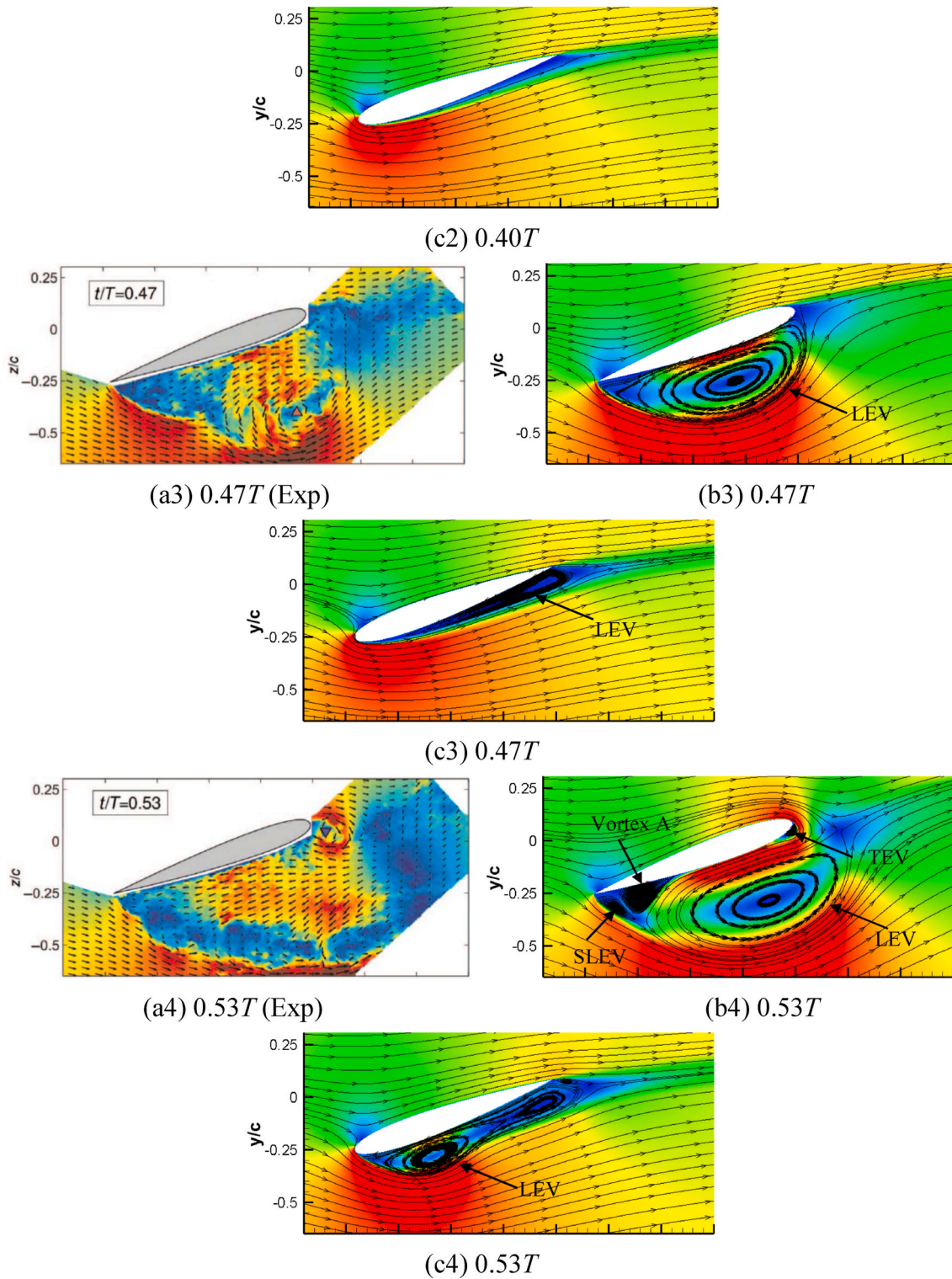(c2) 0.40T

(a3) 0.47T (Exp)

(b3) 0.47T

(c3) 0.47T

(a4) 0.53T (Exp)

(b4) 0.53T

(c4) 0.53T

Fig. 7. (*continued*).

a vertical-axis wind turbine, Rezaeiha et al. (2017) adopted the 4-equation transition SST model and observed that a variable-pitch VAWT can achieve a 6.6% increase of the power coefficient. Additionally, Rezaeiha et al. (2019) found that only the SST model variants has the capability to obtain the reasonable results compared with the experiments, and the transitional SST k-ω versions are recommended in the transitional flow regime. Compared with the original SST k-ω model, Almohammadi et al. (2015) observed that the dynamic stall is very sensitive to the transition

modelling and the existence of the small laminar separation bubble is beneficial to the accurate performance prediction. By using the SA (Spalart–Allmaras) $\gamma - \overline{Re_{\theta t}}$ model, Lind et al. (2014) analyzed the internal flow field of a 2-bladed cycloidal rotor in detail and the main results reveal that the blade-wake interaction is closely associated with force peaks in the predictive instantaneous blade forces. Due to such devices always operating at moderate and low Reynolds numbers, thus, it is necessary to consider the laminar-turbulence transition. However,

(a5) $0.61T$ (Exp)

(b5) $0.61T$

(c5) $0.61T$

(a6) $0.63T$ (Exp)

(b6) $0.63T$

(c6) $0.63T$

(a7) $0.76T$ (Exp)

(b7) $0.76T$
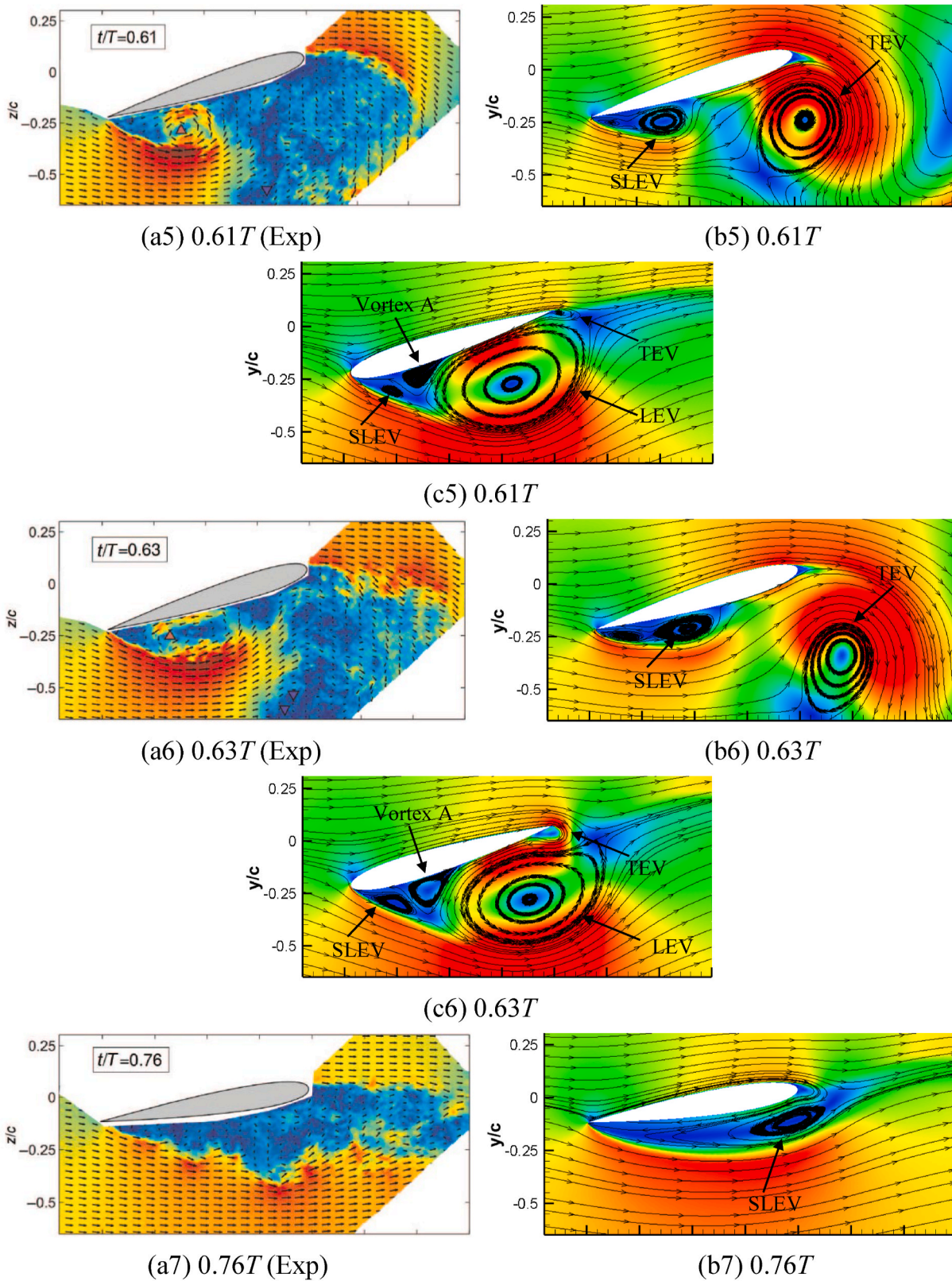
Fig. 7. (*continued*).

the detailed analysis of the transition because of the dynamic effect is still seldom investigated. By the way, the transition model has high requirement of the mesh distribution and time-step, which should be used economically when considering the computational resources (Marsh et al., 2017).

In a cycle of the rotating rotor with variable-pitch motions, the oscillating airfoils often experience the advancing and retreating sides, characterized by the different placements of the airfoil geometry (Granlund et al., 2016). As the airfoil blunt leading edge confronts with the incoming flows, it is in forward mode, which has been investigated

(c7) 0.76T

(a8) 0.91T (Exp)

(b8) 0.91T

(c8) 0.91T

(a9) 0.97T (Exp)

(b9) 0.97T

(c9) 0.97T

Fig. 7. (*continued*).

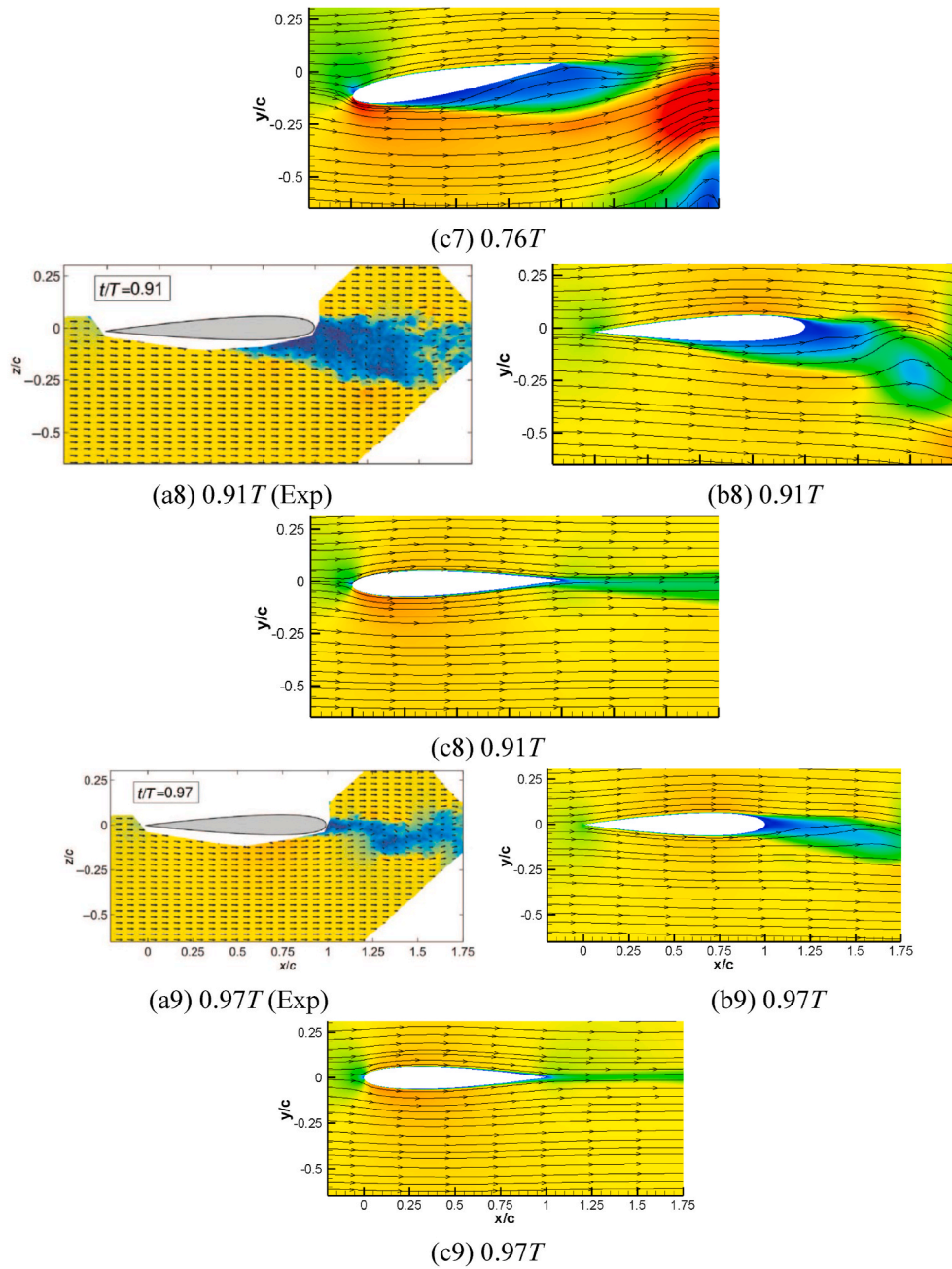widely before. However, when the airfoil is on retreating side, the sharp trailing edge becomes the geometrical leading edge, leading to the obvious change of the blade loading and vortex dynamic. For the static reversed airfoils, Marchand et al. (2017) combined the experiments and computations to clarify the correlation of the lift discontinuity at zero degree with the asymmetry boundary layer between the suction side and pressure side. Moreover, Lind et al. (2016) observed that the thin airfoil with sharp leading edge is weakly sensitive to the Reynolds number while it has the opposite trend for the thick ones. They also conclude that the airloads are strongly dependent of the attack angle (Lind and Jones, 2016a) and the reverse flow wake regimes are determined by the Reynolds number (Lind and Jones, 2015). When it comes to the pitching airfoils, Lind and Jones (2016b) and Hodara et al. (2016) found that the reverse flow dynamic stall is insensitive to the Reynolds number, but has close relationship with the reduced frequency. Besides, Smith and Jones (2019) focused on the effect of the yaw on the strength, number and

behavior of vortices shedding from a pitching airfoil with different kinematics.

According to the aforementioned investigations, it is found that many works are conducted on the forward airfoil/hydrofoil, but rarely on the reversed configuration. Additionally, although some work related to the prediction of the overall performance and unsteady vortex shedding for the reversed pitching airfoils have been done experimentally, the measurement of the transition inside the thin boundary layer is still difficult. As a compensation, with the aid of the numerical methodology, the goal of the present work is to investigate the transitional flows and vortex dynamics over a pitching airfoil operating in reverse mode, with special focus on the parametrical effect. The flow structures around the reversed airfoil are compared with that over the forward one. Meanwhile, the effect of the mean pitching angle and pitching amplitude, reduced frequency and Reynolds number are also taken into consideration. The close relationship between the instantaneous lift coefficient
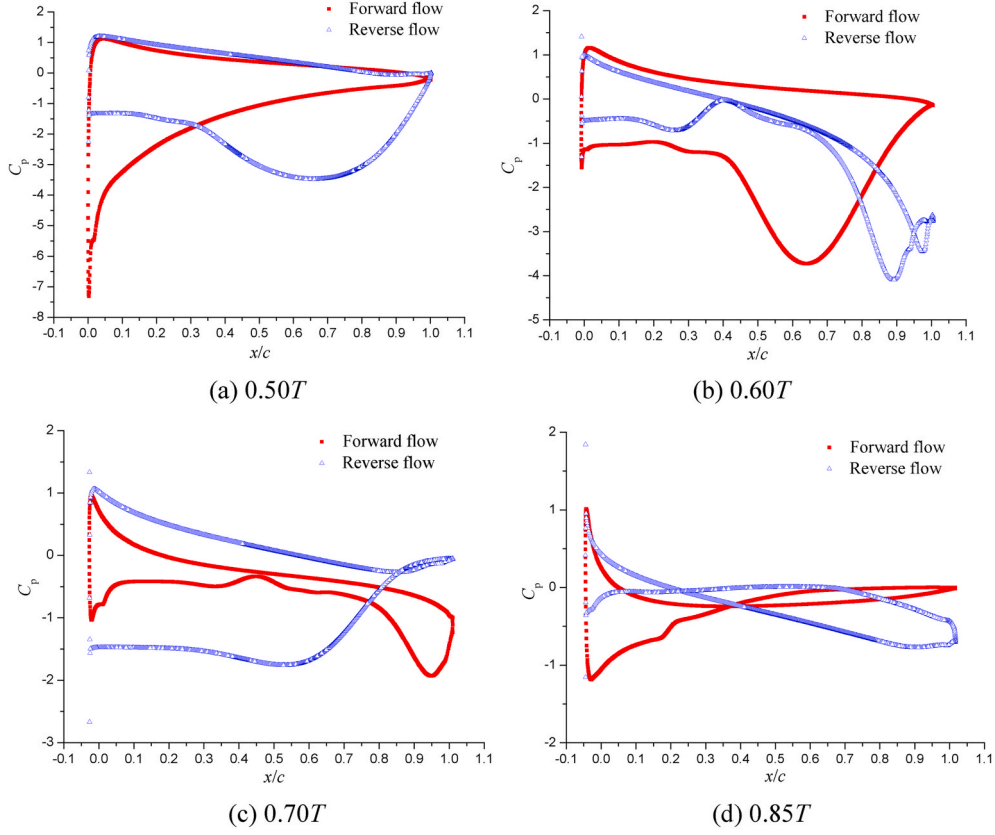
Fig. 8. Pressure distributions at different instants.

variation and the flow filed will be analyzed systematically. It is believed that this work can rich the understandings of the flow physics for the reversed pitching airfoil and shed light on the characteristics of the transition when the airfoil has the moving boundary layer under different working conditions.

2. Turbulence modelling

2.1. SST k-ω turbulence model

A two-equation turbulence model, SST k-ω model, is employed in the present work, because it is widely used in many engineering flows for the moment. This model combines the k-ω model with the k-ε model, in which the near-wall flows are resolved by the former while the latter can deal with the free-stream flows. In addition, the SST k-ω model shows a good behavior in adverse pressure gradients and separating flows (Menter et al., 2003). The turbulent kinetic energy k and specific dissipation rate ω equations are written as follows

$$\frac{\partial(\rho k)}{\partial t} + \frac{\partial(\rho U_j k)}{\partial x_j} = P_k - D_k + \frac{\partial}{\partial x_j}\left[(\mu + \sigma_k \mu_t)\frac{\partial k}{\partial x_j}\right] \tag{1}$$

$$\frac{\partial(\rho \omega)}{\partial t} + \frac{\partial(\rho U_j \omega)}{\partial x_j} = P_\omega - D_\omega + 2\rho(1-F_1)\frac{\sigma_{\omega 2}}{\omega}\frac{\partial k}{\partial x_i}\frac{\partial \omega}{\partial x_i} + \frac{\partial}{\partial x_j}\left[(\mu + \sigma_\omega \mu_t)\frac{\partial \omega}{\partial x_j}\right] \tag{2}$$

$$\mu_t = \frac{\rho a_1 k}{\max(a_1 \omega, SF_1)} \tag{3}$$

where ρ is the fluid density, U_j is the velocity component, P_k and D_k are the production and destruction terms in turbulent kinetic energy equation, μ is the dynamic viscosity, μ_t is the dynamic eddy viscosity, P_ω and D_ω are the production and destruction terms in dissipation rate equation,

S is the characteristic magnitude of the mean velocity gradients and F_1 is the blending function. Other values of the parameters in these two equations can be found in reference (Menter et al., 2003).

2.2. Transition model

The other two equations, namely intermittency γ and transition momentum thickness Reynolds number $\overline{Re_{\theta t}}$, are added to trigger and control the transition region, which are given by

$$\frac{\partial(\rho \gamma)}{\partial t} + \frac{\partial(\rho U_j \gamma)}{\partial x_j} = P_\gamma - E_\gamma + \frac{\partial}{\partial x_j}\left[\left(\mu + \frac{\mu_t}{\sigma_f}\right)\frac{\partial \gamma}{\partial x_j}\right] \tag{4}$$

$$\frac{\partial(\rho \overline{Re_{\theta t}})}{\partial t} + \frac{\partial(\rho U_j \overline{Re_{\theta t}})}{\partial x_j} = P_{\theta t} + \frac{\partial}{\partial x_j}\left[\sigma_{\theta t}(\mu + \mu_t)\frac{\partial \overline{Re_{\theta t}}}{\partial x_j}\right] \tag{5}$$

where P_γ and E_γ are source terms in intermittency equation while $P_{\theta t}$ is the source term in transition momentum thickness Reynolds number equation. The definitions of the correlations and the values of the constants can refer to the references (Menter et al., 2006a, 2006b).

2.3. Coupling the SST k-ω model with $\gamma - \overline{Re_{\theta t}}$ transition model

The coupling of the transition model with the original turbulence model is by the introduction of the effective intermittency γ_{eff} to modify the production and destruction terms in turbulent kinetic energy equation, which is shown by the following formulation

$$\frac{\partial(\rho k)}{\partial t} + \frac{\partial(\rho U_j k)}{\partial x_j} = \widetilde{P_k} - \widetilde{D_k} + \frac{\partial}{\partial x_j}\left[(\mu + \sigma_k \mu_t)\frac{\partial k}{\partial x_j}\right] \tag{6}$$

(a) Pressure coefficient   (b) Skin friction coefficient

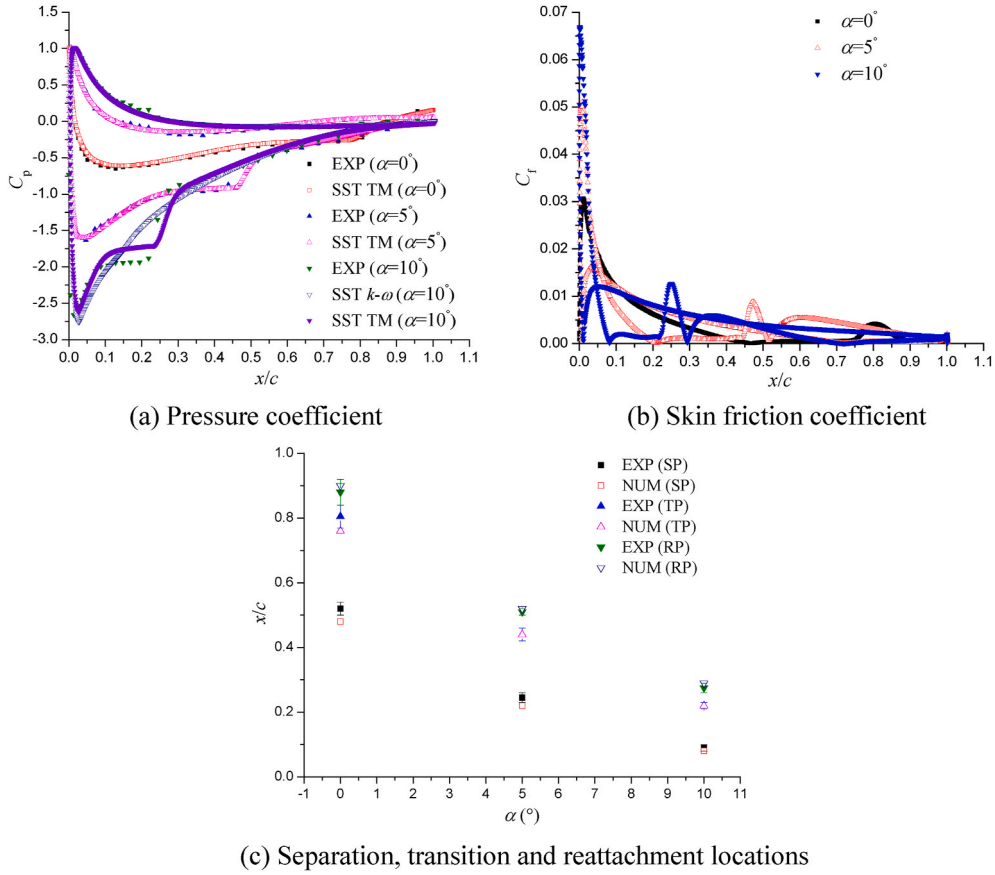(c) Separation, transition and reattachment locations

Fig. 9. Pressure, skin friction coefficients and transition locations at different incidences for a stationary forward airfoil.

$$\frac{\partial(\rho\omega)}{\partial t}+\frac{\partial(\rho U_j\omega)}{\partial x_j}=P_\omega-D_\omega+2\rho(1-F_1)\frac{\sigma_{\omega2}}{\omega}\frac{\partial k}{\partial x_i}\frac{\partial\omega}{\partial x_i}+\frac{\partial}{\partial x_j}\left[(\mu+\sigma_\omega\mu_t)\frac{\partial\omega}{\partial x_j}\right] \tag{7}$$

$$\widetilde{P_k}=\gamma_{eff}P_k \quad \widetilde{D_k}=min\big(max\big(\gamma_{eff},0.1\big),1.0\big)D_k \tag{8}$$

where $\widetilde{P_k}$ and $\widetilde{D_k}$ are the modified production and destruction terms in turbulent kinetic energy equation. The detailed information can be found in related references (Menter et al., 2003, 2006a, 2006b). This transition model has two advantages: the first one is the robustness because of the indirect relationship of the intermittency with the momentum equations while the second is the ability to predict the effects of high free-stream turbulence levels on buffeted laminar boundary layers.

3. Tested cases and numerical setup

3.1. Flow configuration and boundary conditions

The rigid two-dimensional airfoil NACA0012 with the chord length c = 0.203m is adopted in the present work and the corresponding chord Reynolds number is $Re = 1.65 \times 10^5$. The whole computational domain extends 3c from the airfoil leading edge and 10c from the trailing edge. In the pitchwise direction, the top-wall and bottom-wall have the same distance of 4c from the chord line when the airfoil has the incidence of 0°. To control the airfoil movement, the sliding mesh technique in STARCCM+ was employed by creating an interface between the rotating part and the outside stationary region. Both for the forward and reversed pitching airfoils, the pitch-pivot-point is always located at $x = 0.75c$ from the sharp leading edge which is consistent with the experimental setup (Hodara et al., 2016). The experiments were conducted in a low-speed wind tunnel in University of Maryland. The time-resolved

particle image velocimetry (PIV) was applied to measure the instantaneous velocity filed of the reversed pitching airfoil. The reversed airfoil with a nearly sinusoidal pitching is controlled by a 4-bar linkage driven by a motor. The freestream turbulence intensity Tu is approximately 3%, which was used in this work.

Simulations including 2D, incompressible, constant density and unsteady flows are performed in this study. The second-order accuracy is adopted for the convection scheme and temporal discretization, and the diffusion term is discretized by the second-order central differencing. For the boundary conditions, a constant velocity is imposed on the inlet section while the static pressure is assigned on the outlet section. The top-wall and bottom-wall are set as the symmetry planes to eliminate the effect of the sidewall in the pitch-wise direction. The airfoil surface is defined as the no-slip wall. To get a better convergence, the total number of the rotation is 10 and the results in the last cycle are used to analyze the flow structures.

3.2. Mesh generation and validation

When it comes to the mesh generation, the trimmed mesh is employed to the outside region and the prism layer cell is placed near the airfoil surface. Then, the mesh is refined in the rotating part and in the wake region, as shown in Fig. 1. Besides, the growth rate of the mesh keeps the same for all the tested cases with the value of 1.2. The mesh in the wall normal direction is critical to capture the transition and vortex shedding from the airfoil. Therefore, three sets of meshes are tested by changing the prism layer thickness and the number of the layers, which are displayed in Table 1. Simultaneously, the mesh in the streamwise direction is also refined by changing the target size of the mesh near the airfoil surface. Consequently, the resultant y^+ ($y^+ = yu_\tau/\nu$, where y is the distance to the wall, u_τ is the friction velocity and ν is the kinetic
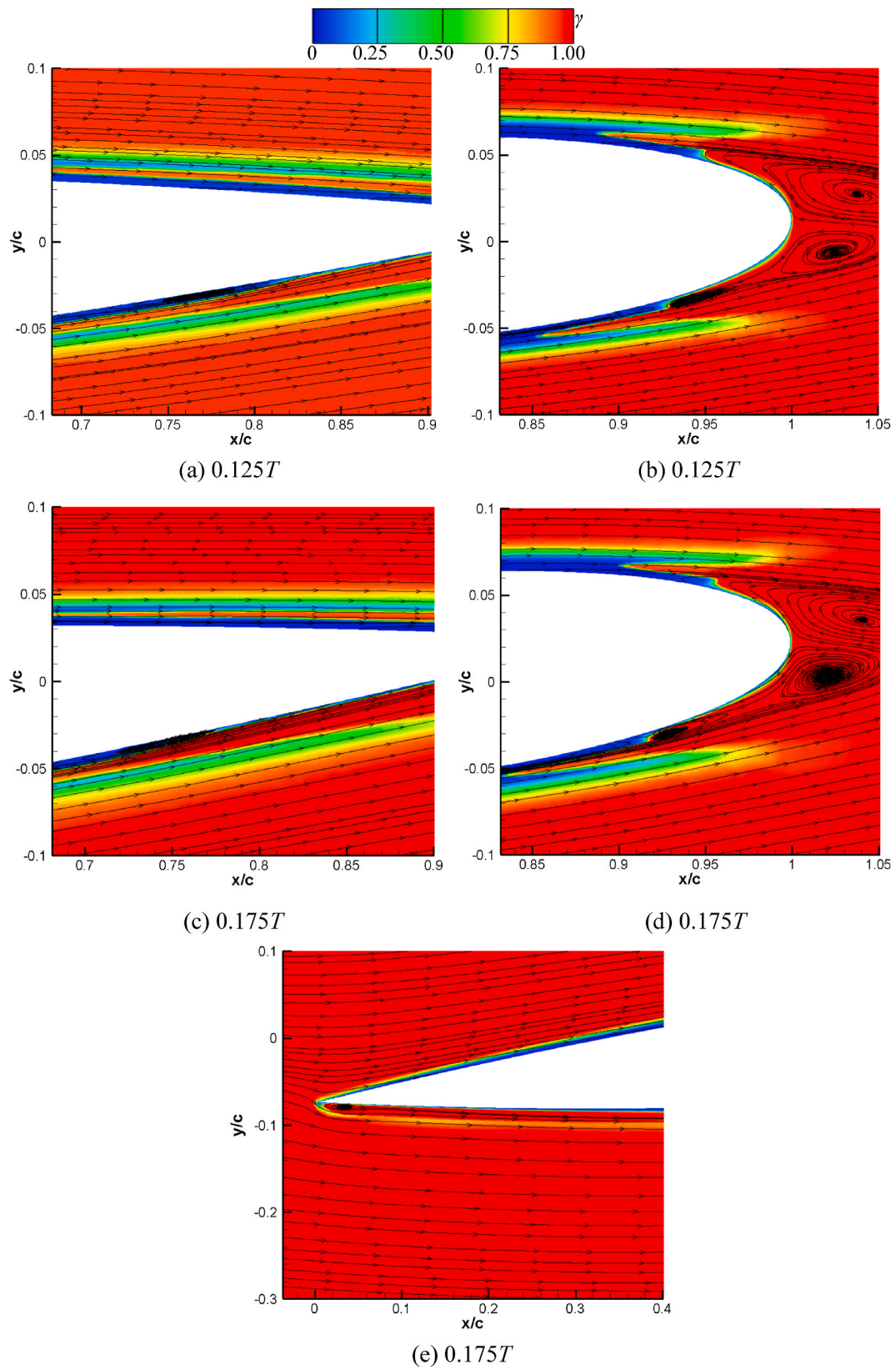
Fig. 10. Intermittency contours with streamlines at different instants. (a), (c) and (f) Forward airfoil; (b), (d) and (h) Trailing edge of the reversed airfoil; (e) and (g) Leading edge of the reversed airfoil; (i) Reversed airfoil.
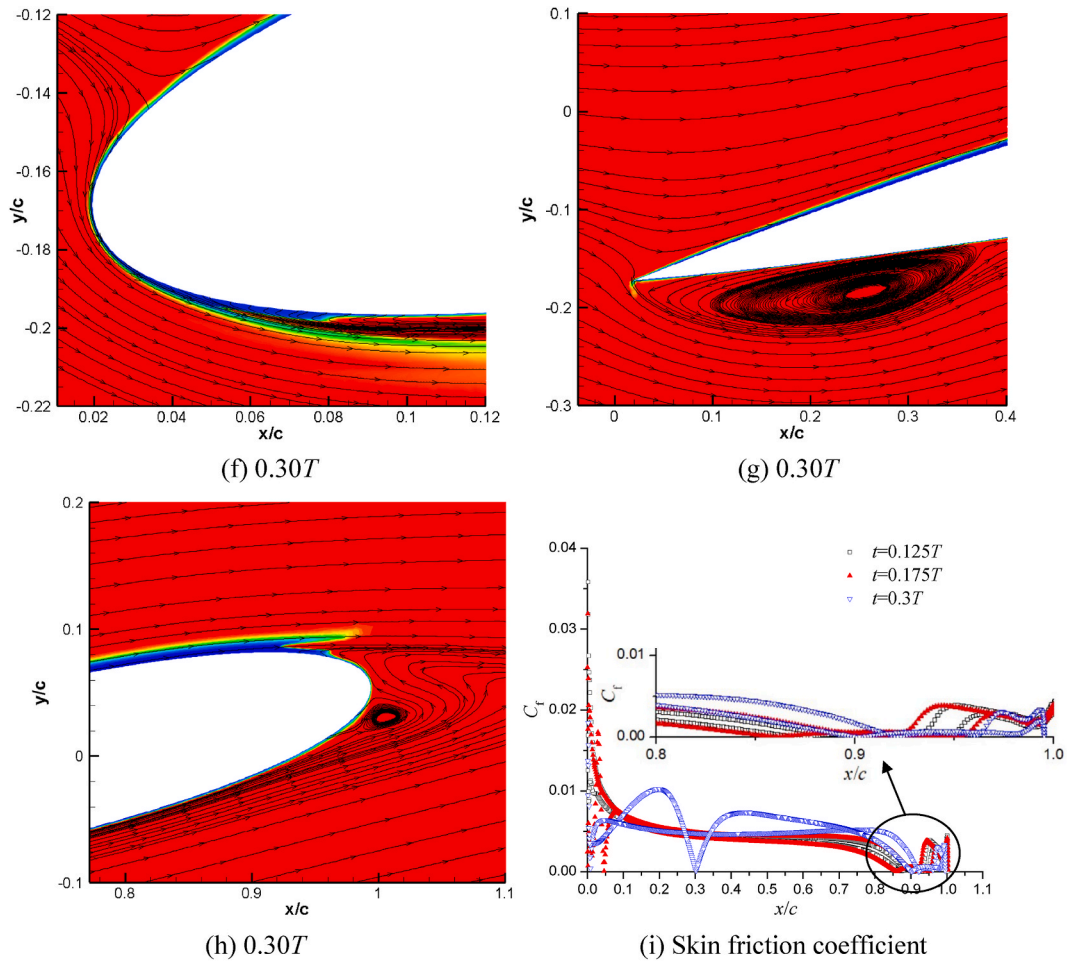
(f) 0.30T

(g) 0.30T

(h) 0.30T

(i) Skin friction coefficient

Fig. 10. (*continued*).

Table 3
Tested cases with different mean pitching incidences and pitching amplitudes.

	Mean pitching angle (°)	Pitching amplitude (°)	Reduced frequency
Case 1	−4	5	0.16
Case 2	−9	5	0.16
Case 3	−10	10	0.16
Case 4	−14	10	0.16

viscosity) decreases by increasing the mesh near the wall. In Table 1, the maximal y^+ is obtained when the airfoil has the attack-of-angle of $0°$. In addition, the distribution of y^+ for mesh 2 on reversed airfoil surface at the maximal incidence is plotted in Fig. 2. It is observed that the maximal y^+ is below 0.2 and it appears near the leading edge where the flow accelerates and separates.

The validation case follows the pitching kinematic shown in Fig. 3a, which is defined as $\theta = -10° + 10° \sin(2\pi f t + \pi/2)$ (where θ is the instantaneous incidence and f is the pitching frequency). The reduced frequency defined as $k = \frac{\pi f c}{U_0}$ (where U_0 is the inflow velocity) is 0.16. The

(a) Pitching kinematics
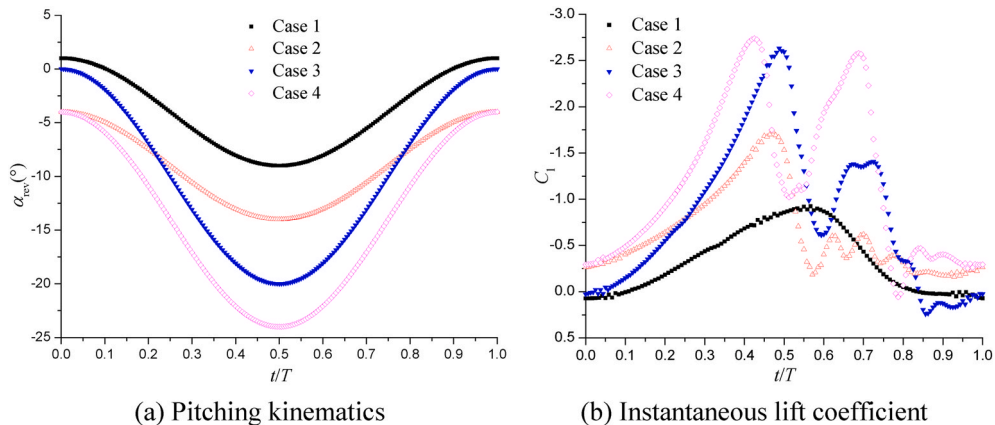

(b) Instantaneous lift coefficient

Fig. 11. Pitching kinematics and instantaneous lift coefficients of four cases.
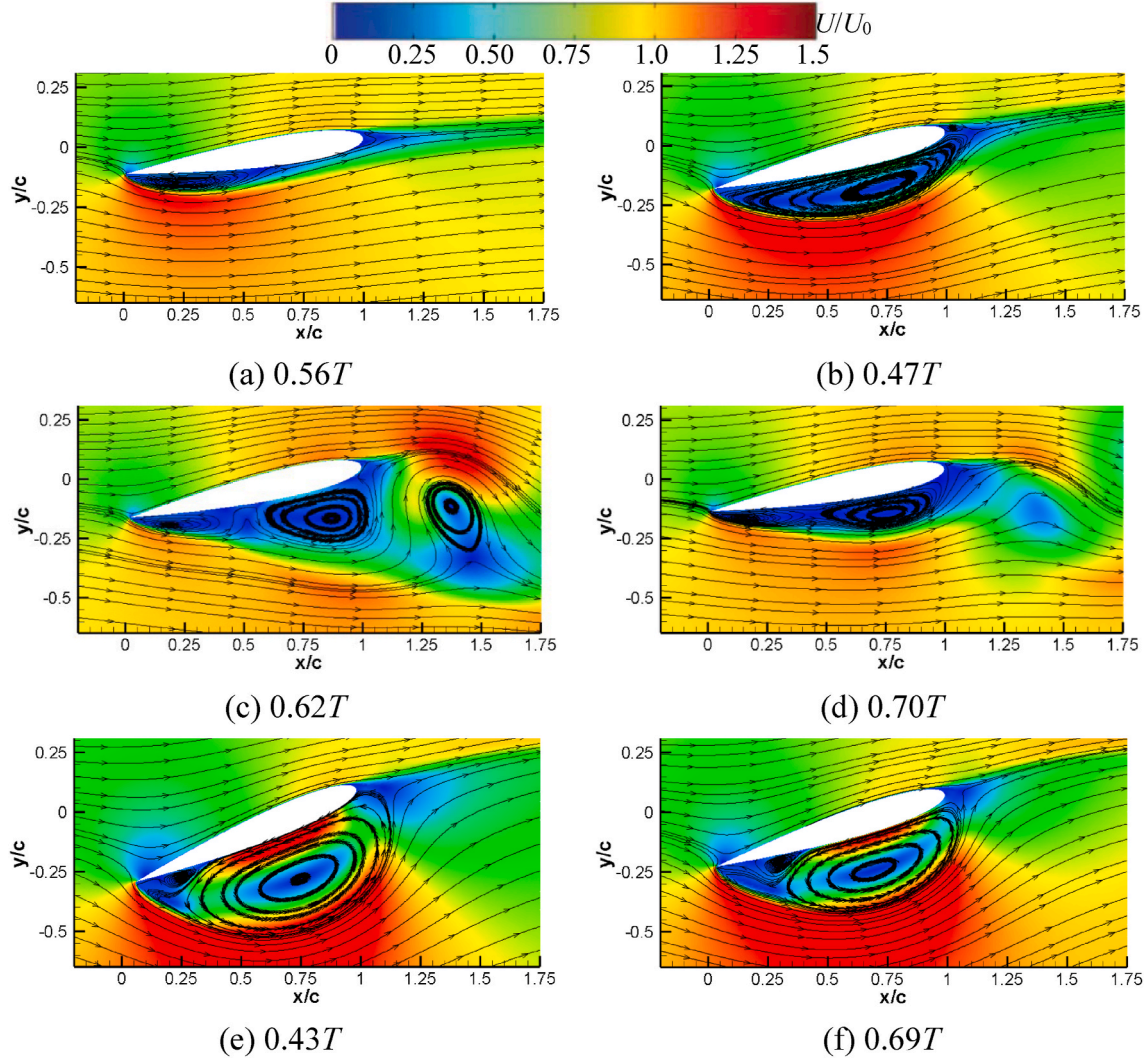
Fig. 12. Vortex structures of various cases at maximal performance. (a) Case1; (b), (c) and (d) Case 2; (e) and (f) Case4.

effect of the mesh resolution on the instantaneous lift coefficient in a rotating cycle is presented in Fig. 3b. Compared with the experiment (Hodara et al., 2016), it seems that the present work shows a reasonable agreement when the airfoil is in the upstroke process, but the peak of the lift coefficient is a little bit delayed in the experiment. Besides, there is a relatively large discrepancy at downstroke stage, which is strongly associated with the three-dimensional effect (Martinat et al., 2008). Then, in Fig. 4, the pressure ($C_p = p/(0.5\rho U_0^2)$, p is the local pressure) and skin friction ($C_f = \tau_w/(0.5\rho U_0^2)$, τ_w is the wall shear stress) coefficients for different meshes are plotted. It can be seen that the difference mainly exists near the blunt trailing edge where the transition occurs. However, the results obtained by mesh 2 and 3 are quite similar, compared with that predicted by mesh 1, due to the sufficient resolution of the near-wall flow.

To further investigate the mesh convergence, Richardson extrapolation method, proposed by Richardson (Richardson and Gaunt, 1927), was used in this work. For a convergence study, at least three different grid resolutions are necessary (Stern et al., 2001). The pth order methods are introduced by Roache (1994), to generalize the Richardson Extrapolation, which is expressed as follows:

$$f_{exact} \approx f_1 + [(f_1 - f_2)/(r^p - 1)] \tag{9}$$

The grid refinement ratio r is defined by the $r = \sqrt{N_{refine}/N_{coarse}}$, where N is the total number of the grid (Celik et al., 2008).

As stated by Stern (Stern et al., 2001), the order of the accuracy can be estimated by using the following equations:

$$p = \frac{\ln(\varepsilon_{21}/\varepsilon_{32})}{\ln(r)} \tag{10}$$

$$\varepsilon_{i+1,i} = f_{i+1} - f_i \tag{11}$$

To evaluate the extrapolated value from these solutions, the convergence of the system must be firstly determined, which are shown as follows: (1) Convergence: $0 < R < 1$; (2) Divergence: $R > 1$. Where R the convergence ratio and it is defined as $R = \varepsilon_{32}/\varepsilon_{21}$.

The grid convergence index (GCI) defines a uniform measurement of the grid refinement convergence. The GCI is derived from the estimated fractional error obtained from the generalization of Richardson extrapolation, and its value represents the resolution level and how much the solution approaches the asymptotic value. The calculated GCI for the fine grid resolutions is presented as follows:

$$GCI_{i+1,i} = F_s |\varepsilon_{i+1,i}|/[f_i(r^p - 1)] \tag{12}$$

Where the factor F_s has the value of 1.25 recommended by Wilcox (Roache, 1998).

In the present work, the order of the accuracy for the time-averaged lift coefficient is shown in Table 2. It seems that there is a reduction for
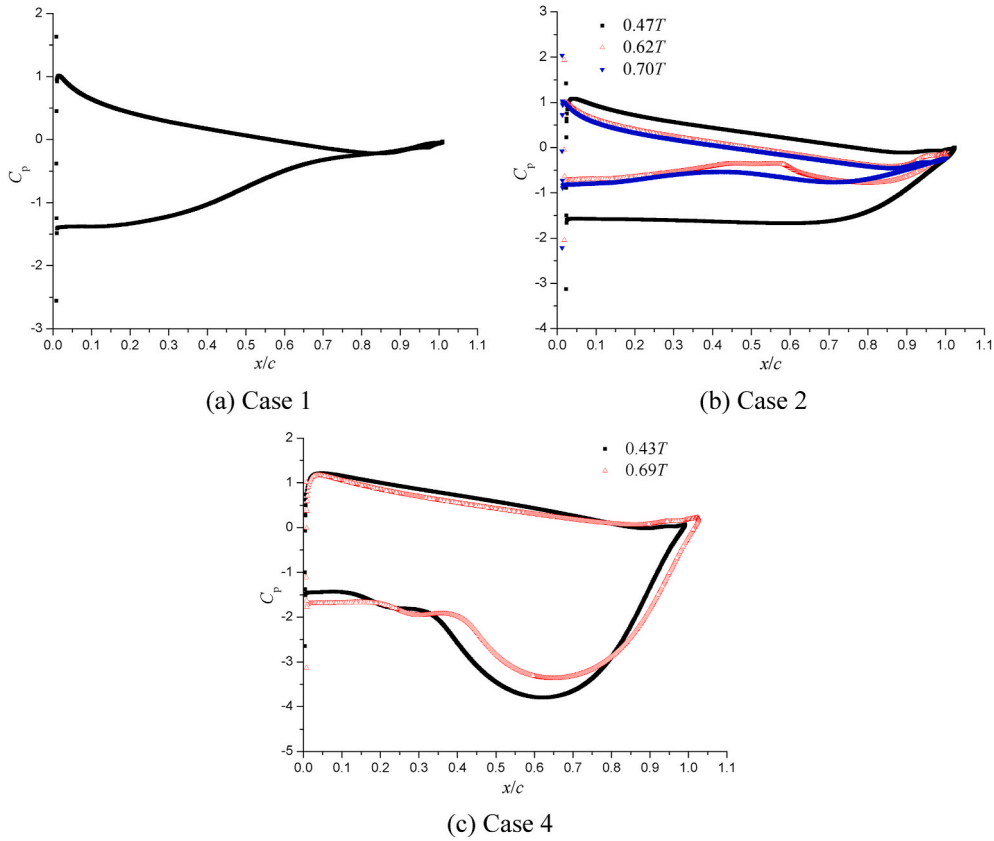
(a) Case 1

(b) Case 2

(c) Case 4

Fig. 13. Pressure distributions of different cases.

three successive grids ($GCI_{32} < GCI_{21}$). The GCI for the finer grid GCI_{32} is much lower than that for the coarse grid GCI_{21}, which indicates that the dependence of the grid resolution is reduced significantly. In addition, it concludes that the grid independent solution is acceptable due to the GCI resolution from the coarse grid to the finer one. Thus, the mesh 2 is appropriate and can be used in the following cases.

3.3. Effect of the time-step

The time-step also has significant influence on the airfoil performance, presented by the instantaneous lift coefficient in a revolution shown in Fig. 5. It can be seen that the time-step has almost no impact on the instantaneous lift coefficient until $t = 0.6T$ (T is the time of a rotating cycle) and then the difference is obvious for different time-steps from $t = 0.6T–0.75T$. By the comparison with the experiment (Hodara et al., 2016), the time-step of $T/160$ achieves a more accurate lift coefficient variation, especially in the downstroke process from $t = 0.6T–0.8T$.

4. Results and discussion

4.1. Flow structures over forward and reversed airfoils

Fig. 6 plots the change of instantaneous lift coefficients in a pitching cycle for forward and reverse airfoils. It is found that the maximal negative lift coefficient of the forward airfoil is smaller than that of the reversed airfoil, but the peak is delayed until $t = 0.6T$, which indicates that the dynamic stall occurs earlier and more violent for the reversed airfoil. Simultaneously, there is a sub-peak of the lift coefficient for the forward and reversed airfoils, respectively. However, the magnitude of the sub-peak is larger and its lifespan is longer when the airfoil operates in reversed mode.

In order to clarify the influence of the vortex evolution on the performance, several instants in a revolution are selected and the results are

compared with the available experimental measurements (Hodara et al., 2016). The velocity magnitude contours along with the streamlines are displayed in Fig. 7. At $t = 0.2T$, flow separation near the sharp leading edge emerges, as well as the wake with the negative velocity near the blunt trailing edge. Then, an obvious structure, leading edge vortex (LEV), is generated near the leading edge and it covers nearly half chord of the blade. However, the flow field around the forward airfoil is still smooth. With the development of LEV from $t = 0.4T–0.47T$, it approximately occupies the whole blade surface. At the same time, the flow separation appears over the lower surface of the forward airfoil, leading to the occurrence of a slender LEV at $t = 0.47T$. Afterwards, the LEV on the reversed airfoil starts to shed from the surface and a small trailing edge vortex (TEV) is created. Besides, between the shear layer and LEV, the second LEV (SLEV) and a vortex A are captured. As described by Tseng and Hu (2016), the generation of vortex A is ascribed to the reverse flow from the other surface and the outer flow of LEV. Simultaneously, the slender LEV on the forward airfoil divides into two parts: the first one is near the leading edge and the second small scale is located at the aft part of the airfoil surface. At $t = 0.61T$ and $0.63T$, the LEV completely disappears and the fully developed TEV is leaving away from the trailing edge. Meanwhile, the SLEV connecting with the shear layer grows quickly for the reversed airfoil. On the forward airfoil surface, a large-scale LEV is apparent by integrating the small scale near the trailing edge and a TEV also appears at the same time. In addition, in the region between the shear layer and LEV, a vortex A and SLEV are also observed. Furthermore, at next instant of $0.76T$, the TEV vanishes in the picture and the SLEV moves towards the trailing edge. For the forward airfoil, the flow field becomes smooth, indicating that the lifetime of these specific vortices is shorter than that over the reversed airfoil. At last two instants, only a small portion of the unsteady wake can be captured near the trailing edge of the reversed airfoil.

In general, it concludes that the flow structures of the reversed airfoil are more complicated than that over the forward airfoil, because of the
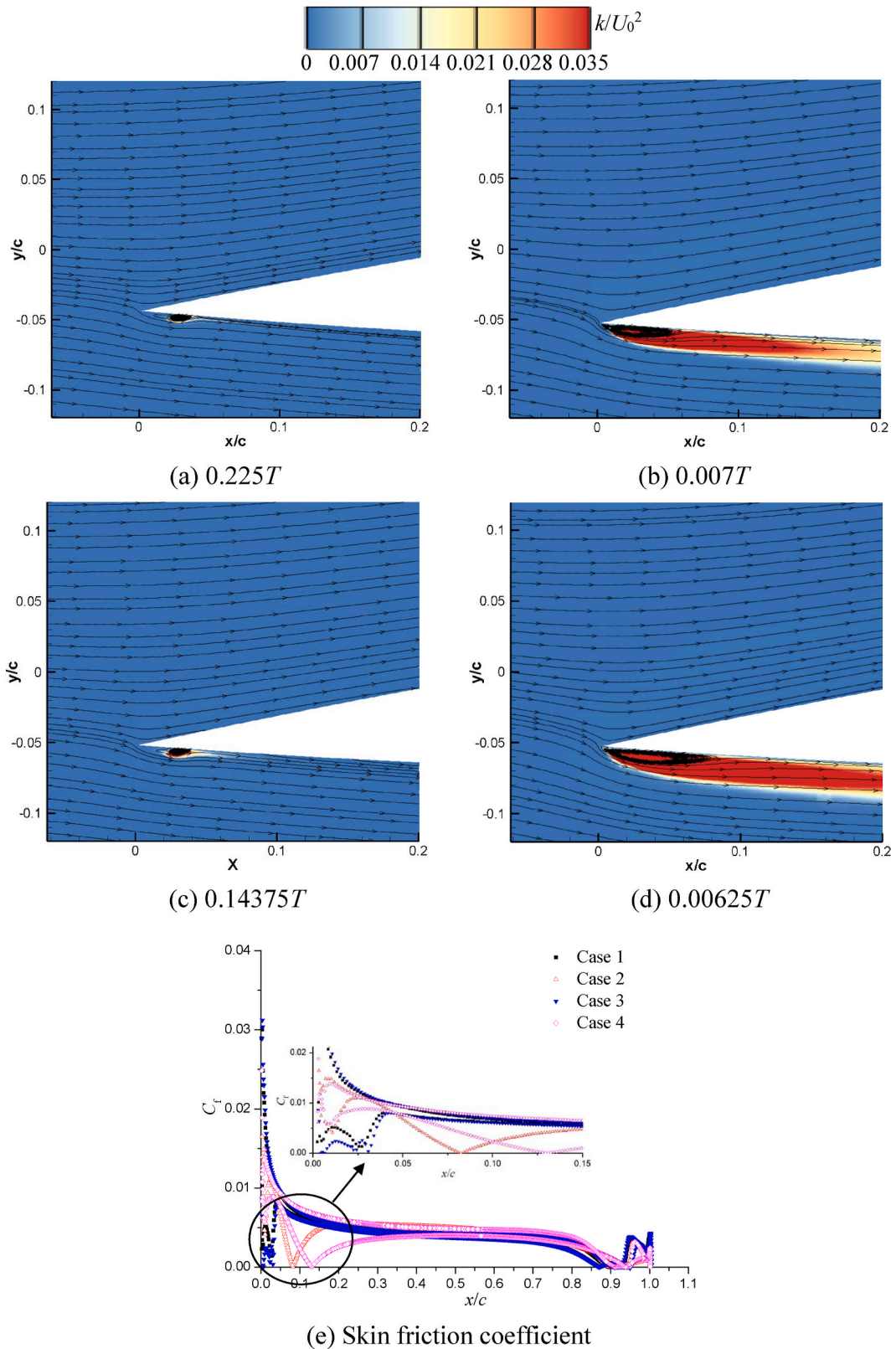
(a) $0.225T$ (b) $0.007T$

(c) $0.14375T$ (d) $0.00625T$

(e) Skin friction coefficient

Fig. 14. TKE and skin friction distributions of different cases. (a) Case 1; (b) Case 2; (c) Case 3; (d) Case 4.

earlier flow separation near the sharp leading edge, which is responsible for the peak of the lift coefficient emerging earlier in Fig. 6. The lifespan of LEV and SLEV on the reversed airfoil is also longer and their influence on the instantaneous lift coefficient is more obvious. Although the trajectory and intensity of various vortices are quite different, the vortex structure evolution is almost the same for the forward and reversed airfoils. By the way, it is observed that some discrepancy still exists between the computations and experiments, for example, the vortex evolution over the reversed airfoil after $t = 0.47T$. At this moment, the lift coefficient reaches to a peak at the stall angle and then the reversed
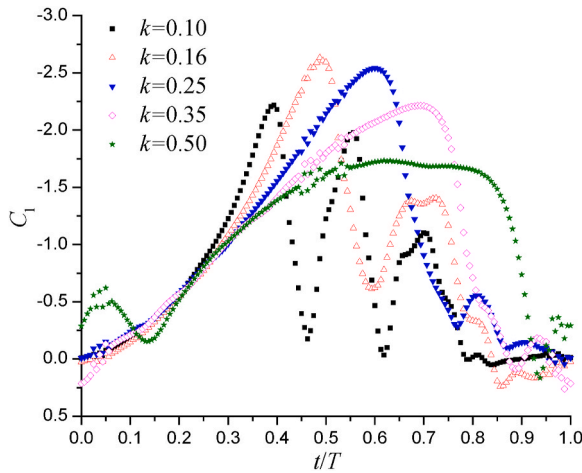
Fig. 15. Instantaneous lift coefficient in a revolution at different k.

airfoil starts to undergo the downstroke process, which has a strong correlation with the three-dimensional effect (Martinat et al., 2008).

To understand the effect of vortex evolution on the airfoil performance, the instantaneous pressure distributions of forward and reversed airfoils are plotted in Fig. 8. At $t = 0.50T$, the reversed airfoil has the maximal negative lift coefficient, which is mainly induced by the development of LEV, which almost occupies the whole blade lower surface. But for the forward airfoil, it seems that the slender LEV structure shown in Fig. 7c3 has no obvious impact on the pressure of the lower surface. However, in the next instant, the main contributor affecting the performance of the forward airfoil is the developed LEV, leading to the significant change of the performance. Meanwhile, the developed TEV starts to shed from the trailing edge and it influences the pressure on both sides, causing the performance degradation of the reversed airfoil. At the same time, the SLEV is growing up, which has an impact on the pressure distribution near the leading edge. Then, as shown in Fig. 8c, the SLEV changes the blade loading at middle chord of the reversed airfoil. At this moment, the pressure distribution of the forward airfoil is quite similar with that of the reversed airfoil at $t = 0.60T$, which is induced by the development and shedding of TEV. Finally, the reversed airfoil has a positive lift coefficient at $t = 0.85T$, shown by a large portion of the positive pressure difference between the upper and lower surfaces.

Then, the laminar-turbulence transition over the forward and reversed airfoils would be discussed in detail. However, due to the limitation of available experiments about the transition on the reversed airfoil, thus, the transition on the stationary forward airfoil at different incidences is firstly used to evaluate the accuracy of the simulation. In Fig. 9, the transition over a NACA0018 airfoil surface is investigated by presenting the pressure and skin friction coefficients, as well as the separation (SP), transition (TP) and reattachment points (RP). The computational results are compared with the experiment (Boutilier and Yarusevych, 2012), which was performed in an open wind tunnel in University of Waterloo. According to the pressure distributions, it seems that the results obtained by the SST transition model (SST TM) match the experiments well, even at relatively high incidence. However, the original SST k-ω model only resolves the fully turbulent flow. Then, with the combination of the skin friction coefficients and transition locations at various incidences, it is observed that the transition shifts upstream as the angle-of-attack increases, especially for the reattachment point, which is more easily affected by the adverse pressure gradient. In addition, due to the evident movement of the reattachment point, the length of LSB becomes short with the increase of the incidence. Generally, compared with the experiments, the computations capture the transition event well, which can be used to validate the applicability of the numerical code and the mesh distribution.

Followed by the analysis of the transition on the stationary airfoil, the main feature of the transition over the forward and reversed pitching airfoils are clarified in this section. If the airfoil has relatively low incidence, there is no evident flow separation and the transition is the primary contributor that affects the blade loading. Therefore, the transition over the forward and reversed airfoils during the upstroke process is shown in Fig. 10 using the intermittency contours. If the value of intermittency is zero, it represents the laminar boundary layer. Otherwise, it is the turbulent boundary layer. At $t = 0.125T$, the transition location of the forward airfoil is approximately at $x/c = 0.78$ while it is near the trailing edge for the reversed airfoil. Then, it is observed that the transition moves towards the leading edge from $t = 0.175T$–$0.30T$ for the forward airfoil because of the increase of the relative attack-of-angle. For the reversed airfoil at $t = 0.175T$, the transition location moves a litter upstream. Near the leading edge, the shear layer transition and generation of LEV is evident. It is found that the transition appears firstly within the shear layer due to the sharp leading edge and then the flow reattaches on the lower surface after the LEV, and finally it occurs near the trailing edge again. As the incidence further increases in the downstroke, the flow near the leading edge totally separates and the LEV develops towards the blade middle chord. Near the trailing edge, the transition becomes unclear due to the decrease of the laminar boundary layer thickness. The skin friction coefficient in Fig. 10i shows that the reattachment of the separated shear layer moves towards the middle chord section with the increase of the incidence, which depends on the evolution of LEV. Near the trailing edge, the transition on the upper surface moves downstream with the increase of the incidence, but on the lower surface, it moves upstream firstly from $t = 0.125T$–$0.175T$. Afterwards, the flow would not reattach and it becomes totally turbulent as the time increases to $0.3T$.

In a conclusion, the mechanism of the transition on the forward and reversed airfoils are quite different. With the increase of the incidence, the transition location is moving towards the leading edge for the forward airfoil. However, for the reversed airfoil, the transition occurs within the leading-edge separated shear layer and near the trailing edge initially. After that, with the increase of the incidence, the shear layer transition near the leading edge becomes unclear because of the fully turbulent flow induced by the development of LEV. Simultaneously, near the trailing edge, the boundary layer flows on the lower surface become turbulent gradually. However, the length of the laminar boundary layer on the upper surface becomes longer, as shown in Fig. 10h.

4.2. Effect of the mean incidence and pitching amplitude on reverse flow

This section shows the effect of the mean pitching incidence and pitching amplitude on the transition and vortex dynamics on the reversed airfoil. Four cases with same reduced frequency listed in Table 3 are tested and the pitching kinematics are presented in Fig. 11a. Fig. 11b presents the instantaneous lift coefficient variation of four tested cases in a rotating cycle. With the increase of the maximal pitching angle from case 1 to case 4, the peak of the negative lift coefficient also increases. Moreover, the sub-peak of the lift coefficient, induced by SLEV, is more evident for large mean incidence and pitching amplitude. In case 2, two sub-peaks are observed and this trend gradually disappears in case 3 and case 4, but the magnitude of the sub-peak in case 4 is nearly the same with the value of the peak.

The detailed flow structures at several instants where the lift coefficients have the maximal negative values are shown in Fig. 12 for different cases. In case 1, due to the low maximal incidence, the LEV is always attached on the surface and no vortex shedding is observed. But in case 2, one peak and two sub-peaks of the lift coefficient are observed, in which the development of LEV should be responsible for the first one while the other two sub-peaks are associated with the SLEV and third leading edge vortex (TLEV), shown in Fig. 12c and d. Then, in case 4, there are two peaks almost having the same magnitude, indicating that
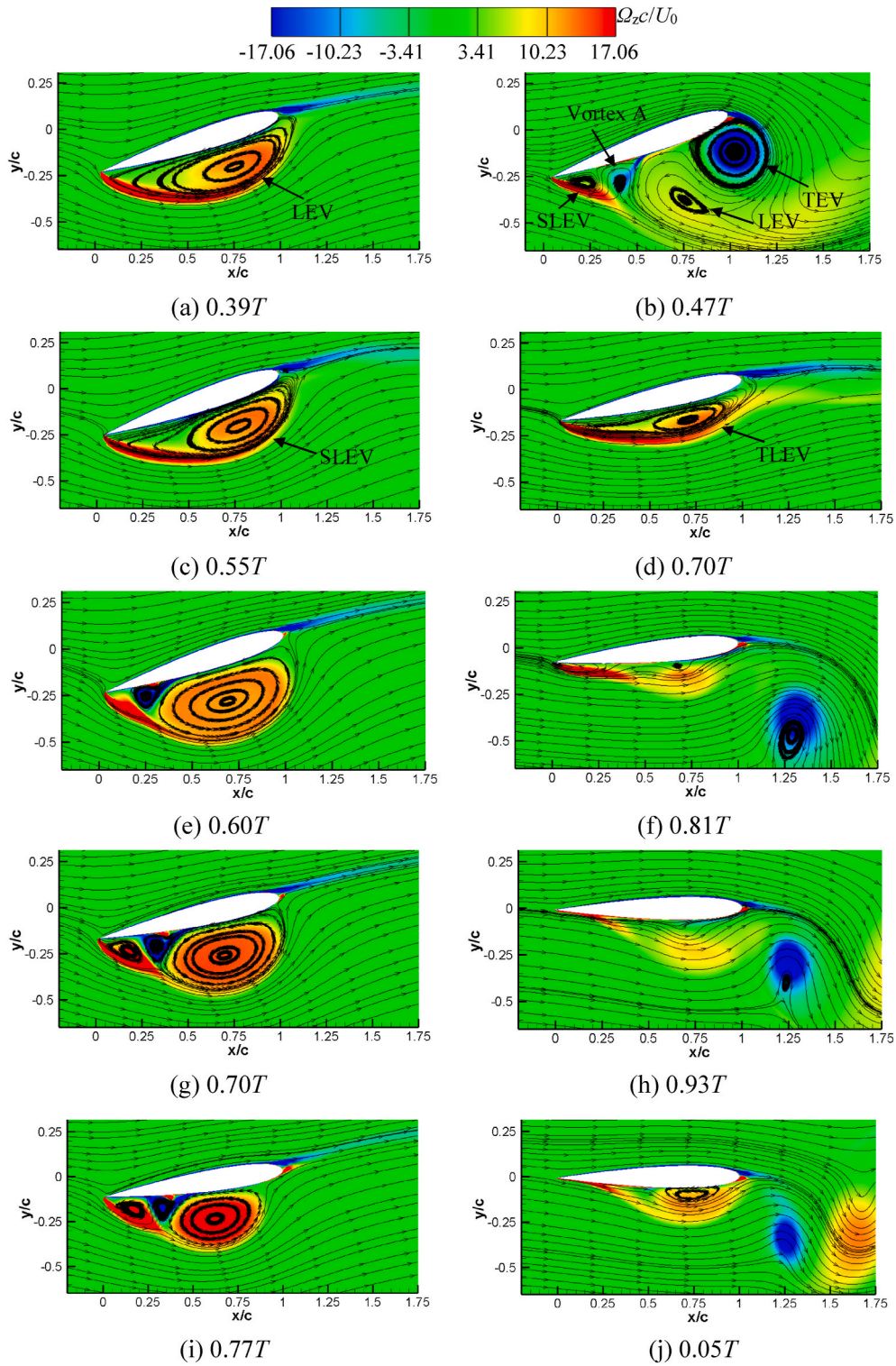
Fig. 16. Flow structures at different instants at various k. (a), (b), (c) and (d) $k = 0.1$; (e) and (f) $k = 0.25$; (g) and (h) $k = 0.35$; (i) and (j) $k = 0.50$.

the SLEV has the same effect on the performance compared with LEV. But the size of SLEV is a little smaller than LEV.

The distributions of pressure coefficients at instants shown in Fig. 11, are plotted in Fig. 13 to show the influence of the vortex evolution on the blade loading. In case 1, the attached LEV near the sharp leading edge has no significant influence on the lower surface pressure, because of the relatively small maximal incidence resulting in the incomplete developed vortex structure. However, in case 2, the fully developed LEV occupies the whole blade surface, leading to the evident change of the

pressure. Meanwhile, although the pressure difference induced by SLEV and TLEV is smaller than LEV, the blade loading at these two instants are nearly the same, which is responsible for the same performance. Finally, the effect of LEV and SLEV on the performance is really obvious in case 4, but the intensity of LEV is a little higher than SLEV.

In Fig. 14, the inception of LEV, visualized by the distributions of turbulent kinetic energy (TKE) and skin friction coefficients, are displayed for different cases. In case 2 and 4, due to the relatively large negative incidence (-4°) in the initial time, the LEV develops at the first
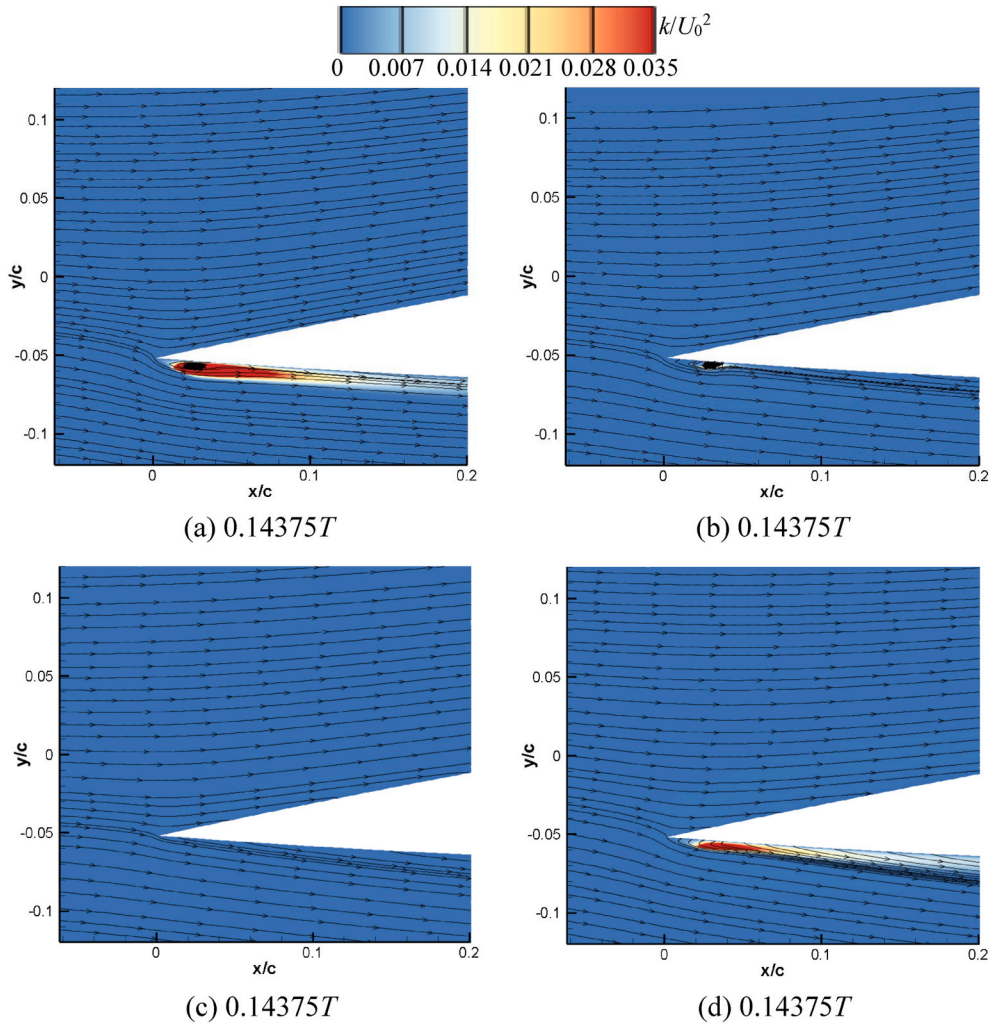
Fig. 17. Leading edge transition at different k. (a) $k = 0.10$; (b) $k = 0.25$; (c) $k = 0.35$; (d) $k = 0.50$.

time and the transition occurs closer to the sharp leading edge than that in case 1 and 3, in which the small-case LEV appears a little downstream from the leading edge. From the distributions of skin friction coefficient, it is observed that the magnitude increases when the transition appears firstly, due to the recirculation flow induced by LEV. The transition locations in case 2 and 4 are more upstream compared with that in case 1 and 3, as a result of the earlier flow separation. At the same time, the reattachment location is more downstream for case 2 and 4, especially for case 4, which indicates that the size of LEV is much larger than that in case 1 and 3.

4.3. Effect of the reduced frequency on reverse flow

In this section, five groups of the reduced frequency, involving 0.10, 0.16, 0.25, 0.35 and 0.50, are investigated systematically, in terms of the vortex dynamics and near-wall flows. Fig. 15 shows the instantaneous lift coefficients in a revolution for different reduced frequency. With the increase of the reduced frequency, the peak of the lift coefficient initially increases from $k = 0.10$ to 0.16 and then it decreases from $k = 0.16$ to 0.50. Simultaneously, it is also delayed, which means that the dynamic stall is also postponed. For $k = 0.10$, there are two obvious sub-peaks at t

$= 0.55T$ and $0.70T$. However, for other cases, there is only one sub-peak. Consistent with the peak of the lift coefficient, the sub-peak is also delayed, even in the next revolution when k is equal to 0.5, indicating that with the increase of k, the LEV can persist for a longer time.

To clarify the effect of the vortex evolution on the performance, the spanwise vorticity contours with streamlines are displayed in Fig. 16 at different instants correspond to the peaks and sub-peaks shown in Fig. 15. When k has the value of 0.1, the peak and sub-peaks of the lift coefficient shown in Fig. 16a, c and 16d are closely associated with the LEV, SLEV and TLEV, but the intensity decreases gradually. In Fig. 16b, the LEV is going to disappear and the TEV develops fully, bringing about the degradation of the overall performance. The vortex A and SLEV, coexisting with the opposite sign of the vorticity, are also observed at this time. Then, with the increase of k from 0.16 to 0.50, there are always three main vortex structures: LEV, vortex A and SLEV, which can maintain the high negative lift coefficient. However, the size of LEV is largest when the reduced frequency is 0.16 (shown in Fig. 7b4). Then, when it comes to the sub-peak of the lift coefficient, it can be seen that the TEV shedding is the main contributor to the high lift coefficient, but the small-scale SLEV is still visible on the lower surface. In a word, with the increase of k, the dynamic stall is delayed as a consequence of the
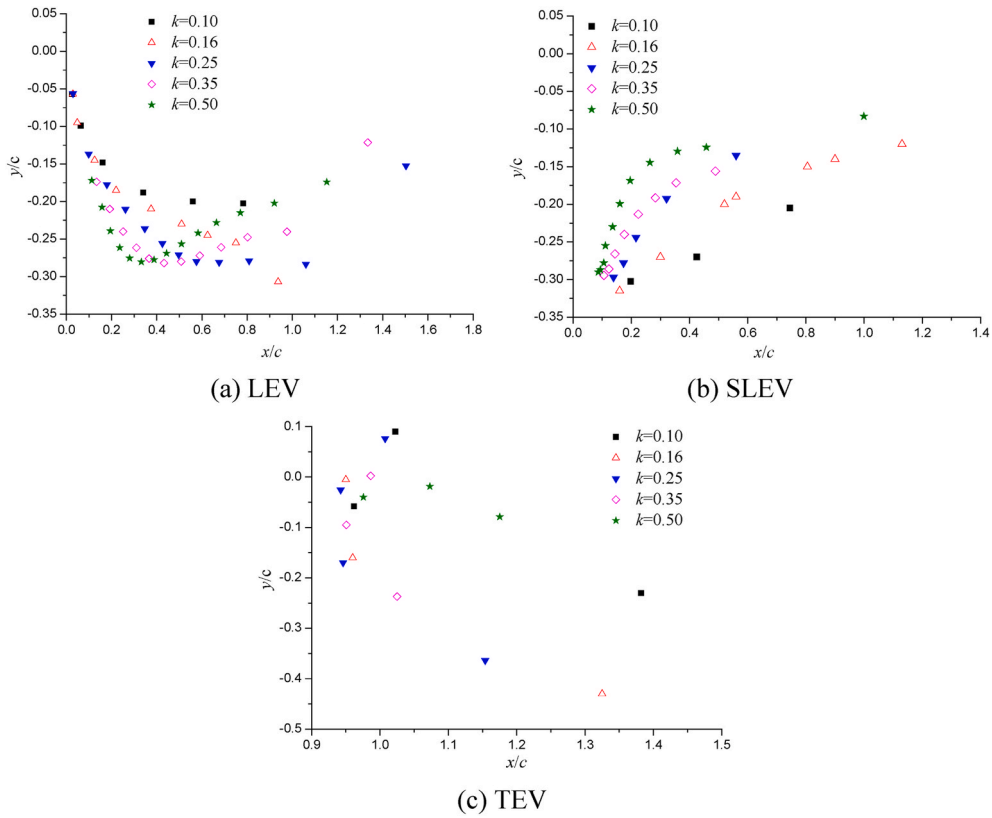
(a) LEV

(b) SLEV

(c) TEV

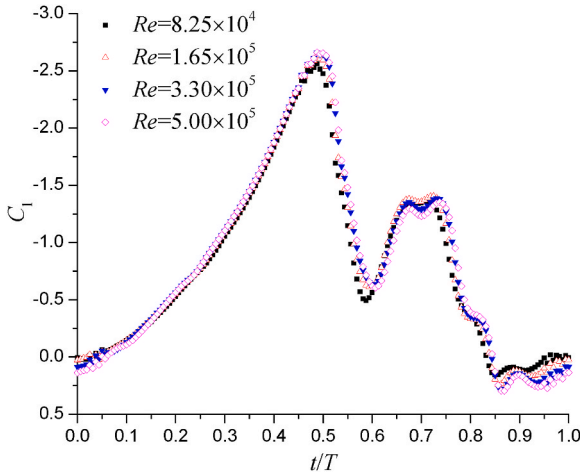**Fig. 18.** Vortex trajectory at different k.

Fig. 19. Instantaneous lift coefficient variation in a revolution at different Re.

delayed vortex generation and development.

Fig. 17 presents the leading-edge transition induced by the generation of LEV, which is shown by the TKE contours coupled with streamlines for various k. With the increase of k from 0.10 to 0.25, the LEV is often attached on the lower surface, but the value of TKE and size of LEV reduces. When k is equal to 0.35, there is no LEV near the sharp leading

edge. Then, for the highest reduced frequency at this instant, the transition region is still visible, but the LEV has already shed and the next one would appear. Generally, with the increase of k, not only is the dynamic stall delayed, but also the transition induced by the LEV generation is also postponed.

The trajectory of three main vortices at different k is traced by identifying the vortex core location using the streamlines, which is shown in Fig. 18. The inception of LEV is very close to the airfoil sharp leading edge and then it moves far away from the lower surface. However, at low reduced frequency of 0.1 and 0.16, the LEV vanishes downstream directly. When k increases from 0.25 to 0.50, the LEV also moves along the direction that approaches to the lower surface near the trailing edge, which is caused by the inertia force as a consequence of the fast pitching possibly. For the motion of SLEV, it initially occurs far away from the leading edge and then moves towards the trailing edge of the lower surface. By the comparison, it is observed that the SLEV at high reduced frequency has the large velocity (the slope of the plot data) and reaches to the lower surface in advance. When the TEV emerges near the blunt trailing edge, it firstly moves forward along the lower surface and then it starts to shed. There has almost no much difference in TEV movement as the reduced frequency increases from 0.16 to 0.35. Obviously, the TEV trajectory obtained at $k = 0.1$ is closer to the lower surface compared with other cases. But at $k = 0.50$, it seems that the TEV has no time to response and convects downstream quickly.

4.4. Effect of the Reynolds number on reverse flow

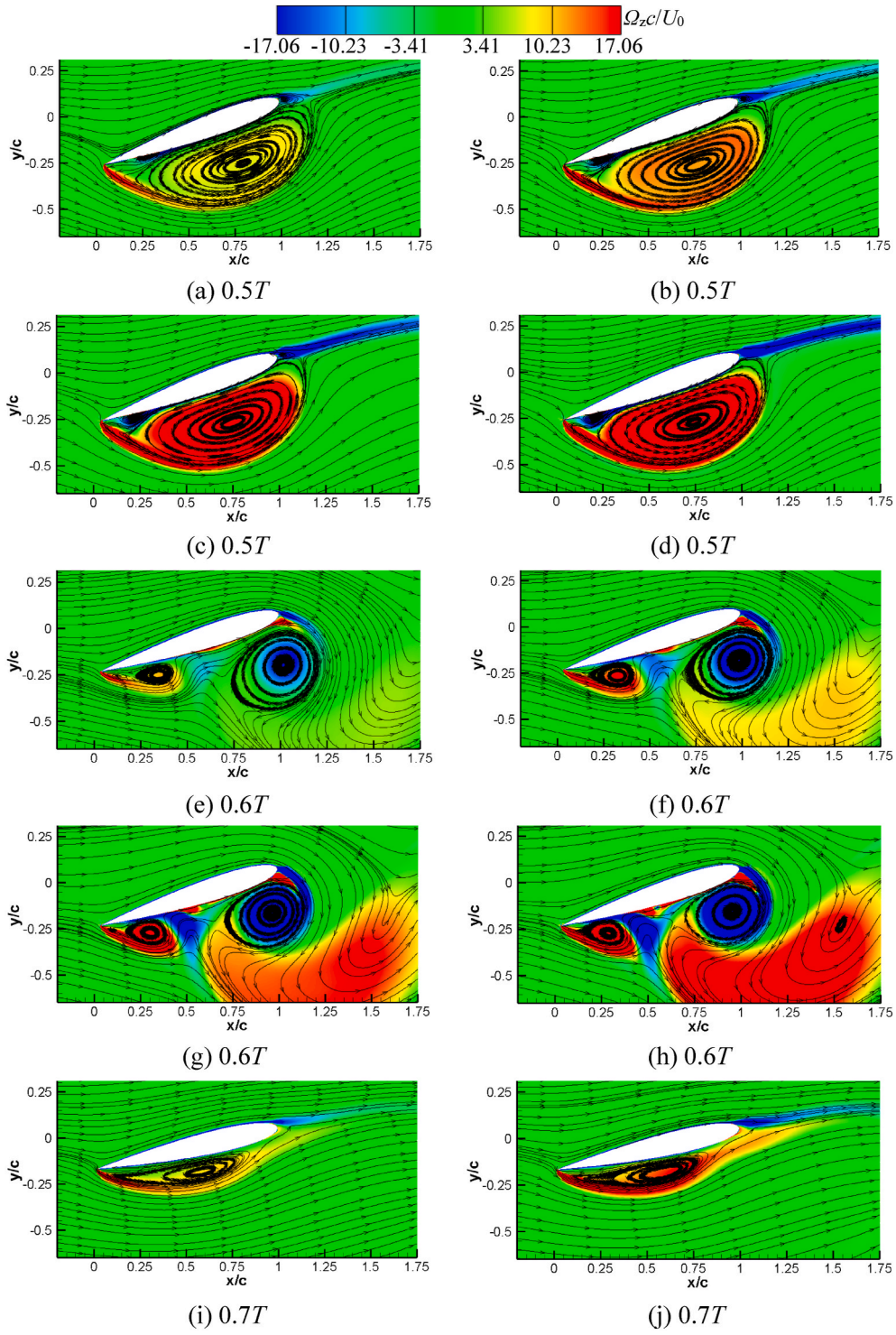The prediction of the instantaneous lift coefficients at different Re is

Fig. 20. Flow structures at several instants at different Re. (a), (e), (i) and (m) $Re = 8.25 \times 10^4$; (b), (f), (j) and (n) $Re = 1.65 \times 10^5$; (c), (g), (k) and (o) $Re = 3.30 \times 10^5$; (d), (h), (l) and (p) $Re = 5.00 \times 10^5$.

shown in Fig. 19. It seems that there is almost no difference in lift co-efficient obtained at various Re in the upstroke process until $t = 0.5T$. However, in the period of the downstroke, a small difference is still evident, which should be clarified in detail by analyzing the flow structures.

Four instants, including $t = 0.5T$, $0.6T$, $0.7T$ and $0.85T$, are selected to compare the flow structures at various Reynolds numbers. The spanwise vorticity component with the streamlines are shown in Fig. 20.
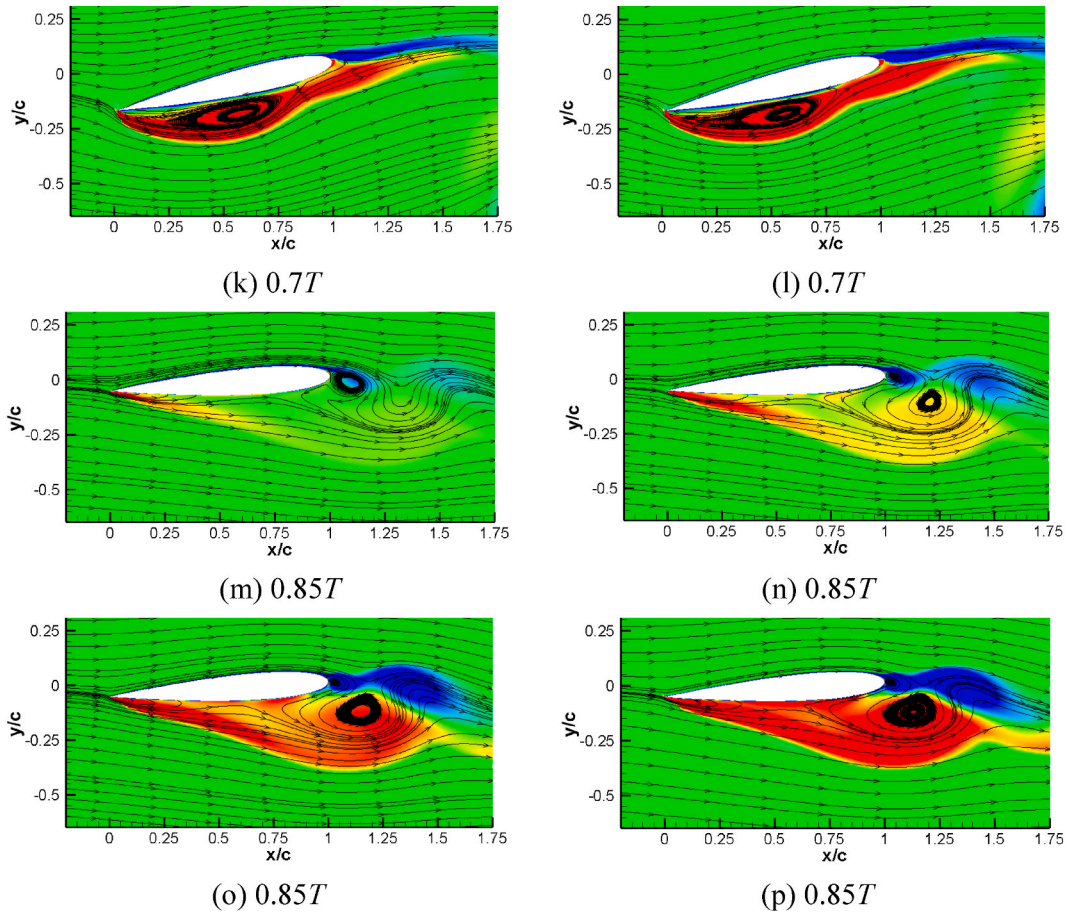
(k) $0.7T$

(l) $0.7T$

(m) $0.85T$

(n) $0.85T$

(o) $0.85T$

(p) $0.85T$

Fig. 20. (*continued*).

At $t = 0.5T$, the reversed airfoil has the maximal lift coefficient and the whole lower surface is almost occupied by the LEV. At the same time, the vortex A and TEV with small size are also evident. With the increase of Re, the intensity of LEV becomes stronger, as well as the vortex A and TEV. Then, at next instant $t = 0.6T$, the LEV has already shed and the main flow structure is dominated by SLEV and TEV. However, the shedding LEV with positive vorticity is still visible downstream at $Re = 5 \times 10^5$. In this moment, due to the developed TEV and shed LEV, the performance of the reversed airfoil is deteriorated, which can also be seen in Fig. 8b. With the development of SLEV, the lift coefficient increases gradually and it reaches to a sub-peak at $t = 0.7T$. Meanwhile, the strength of SLEV is more intensive as the Reynolds number increases. When the airfoil is going to finish a pitching cycle, a small valley occurs at $t = 0.85T$, as a result of the small-scale TEV and shedding SLEV. But at low Reynolds number, the shedding SLEV is not visible in the screen while the TEV has a relatively large size, resulting in the worst performance. Generally, it concludes that the LEV, SLEV and TEV have the stronger intensity with the increase of Re. Simultaneously, the flow field is more complex at high Reynolds number, owing to the large mainstream velocity and the resultant strong vortices.

The transition induced by the inception of LEV near the sharp leading edge at different Re is also compared in Fig. 21 using TKE contours along with streamlines. When the Reynolds number is low, the TKE near the wall region is small due to the low velocity fluctuation. At $Re = 8.25 \times$

10^4, the transition is unclear because it is extremely close to the sharp leading edge. Then, when Re increases, the transition and reattachment points move downstream. However, as the Reynolds number increases to 5×10^5, the transition and reattachment points shift upstream. As a result, the size of LEV in these two cases are quite similar.

The trajectory of different vortices at different Re are plotted in Fig. 22, by detecting the location of vortex core region using the streamlines. The movement path of LEV and SLEV has the opposite trend, in which the LEV moves away from the lower surface while the SLEV approaches to the lower surface gradually. At relatively low Reynolds number, the LEV disappears near the trailing edge due to the weak intensity and the trajectory of LEV is closer to the airfoil surface. However, at high Reynolds number of 3.3×10^5 and 5.0×10^5, the LEV persists for a longer time and convects more downstream. At the same time, under low Reynolds number condition, the SLEV and TEV move quickly and have a long path, especially for TEV. This phenomenon can be caused by the earlier vortex shedding and the weak integration of the mainstream.

5. Concluding remarks and future work

In the present work, the SST $\gamma - \overline{Re_{\theta t}}$ transition model is applied to simulate the two-dimensional unsteady flows around the rigid forward and reversed pitching airfoil, with special attention to the parametrical
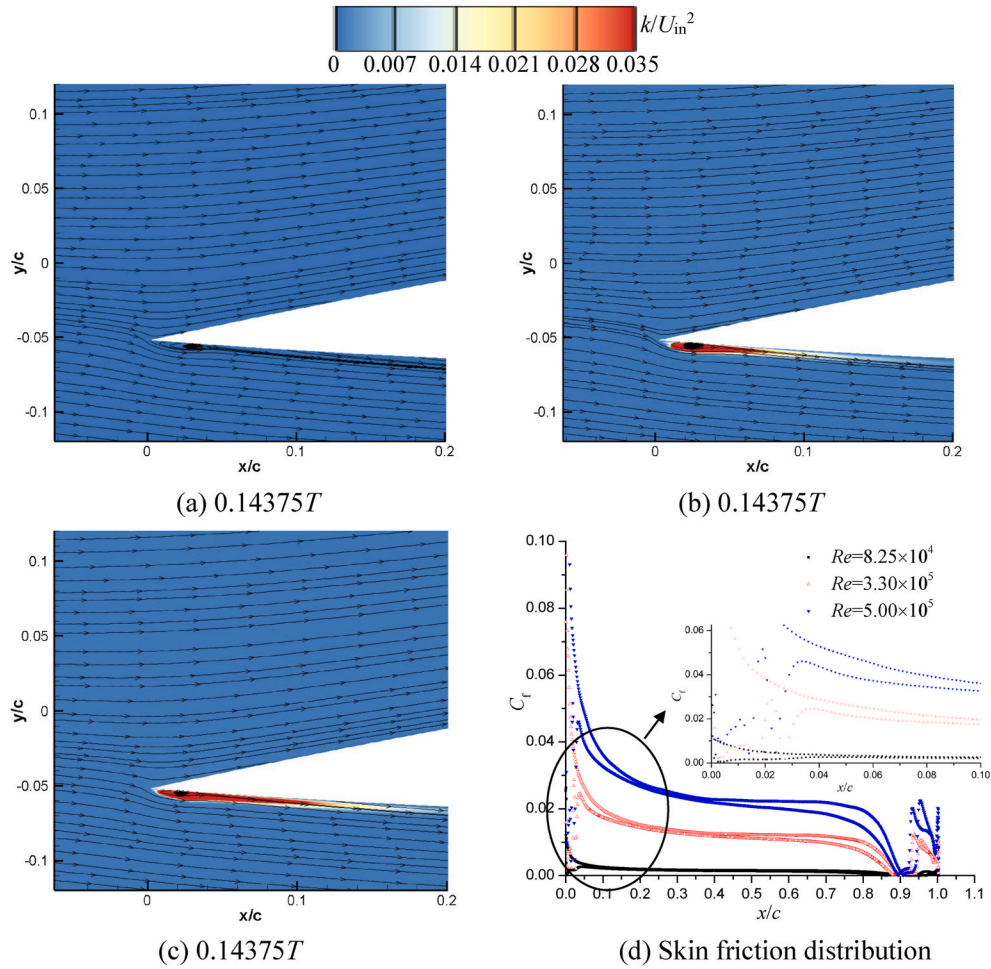
Fig. 21. Distributions of TKE and skin friction coefficients at different Re. (a) $Re = 8.25 \times 10^4$; (b) $Re = 3.30 \times 10^5$; (c) $Re = 5.00 \times 10^5$; (d) Skin friction coefficients.

effect on the global performance and flow structures. The main conclusion is listed as follows:

(1) Compared with the forward airfoil, the flow structures over the reversed airfoil are more complicated and the influence of different vortices on the overall performance is more intensive, as a result of the earlier flow separation near the sharp leading edge. The existence of LEV can maintain the high performance while the development and shedding of TEV is responsible for the performance degradation. The transition on the forward airfoil moves from the trailing edge to the leading edge as the incidence increases. However, for the reversed airfoil, the transition initially appears within the separated shear layer and then reattaches after the LEV. Afterwards, the transition occurs again near the blunt trailing edge. With the increase of the attack-of-angle, the trailing-edge transition on the lower side becomes unclear while it moves downstream on the upper side, leading to the asymmetrical boundary layer.

(2) For the tested cases with large negative mean pitching angle and pitching amplitude, the influence of LEV and SLEV on the performance is more intensive. When the initial pitching angle is

negative with a relatively large value, the induced transition by the developed LEV is closer to the leading edge.

(3) As the reduced frequency increases, it is observed that the dynamic stall and transition are all delayed. At high reduced frequency, the sub-peak of the lift coefficient induced by the SLEV emerges in the next revolution. The trajectory of LEV and SLEV has the opposite trend and the vortices have the large migration velocity with the increase of k.

(4) With the increase of Re, the strength of different vortices is stronger, leading to the long persistence of LEV. The LEV-induced transition is closer to the leading edge and the trailing edge transition also move a little upstream as the Reynolds number increases. For the movement of SLEV and TEV, it is observed that they have a longer path under low Reynolds number condition, which can be ascribed to the earlier flow separation and weak integration of the mainstream.

It should be admitted that the present work still has a large discrepancy with the experiments, especially for the performance and flow structures in the downstroke process due to the limitation of the RANS-based turbulence model and three-dimensional effect. Thus, the hybrid RANS/LES turbulence models or large eddy simulation is
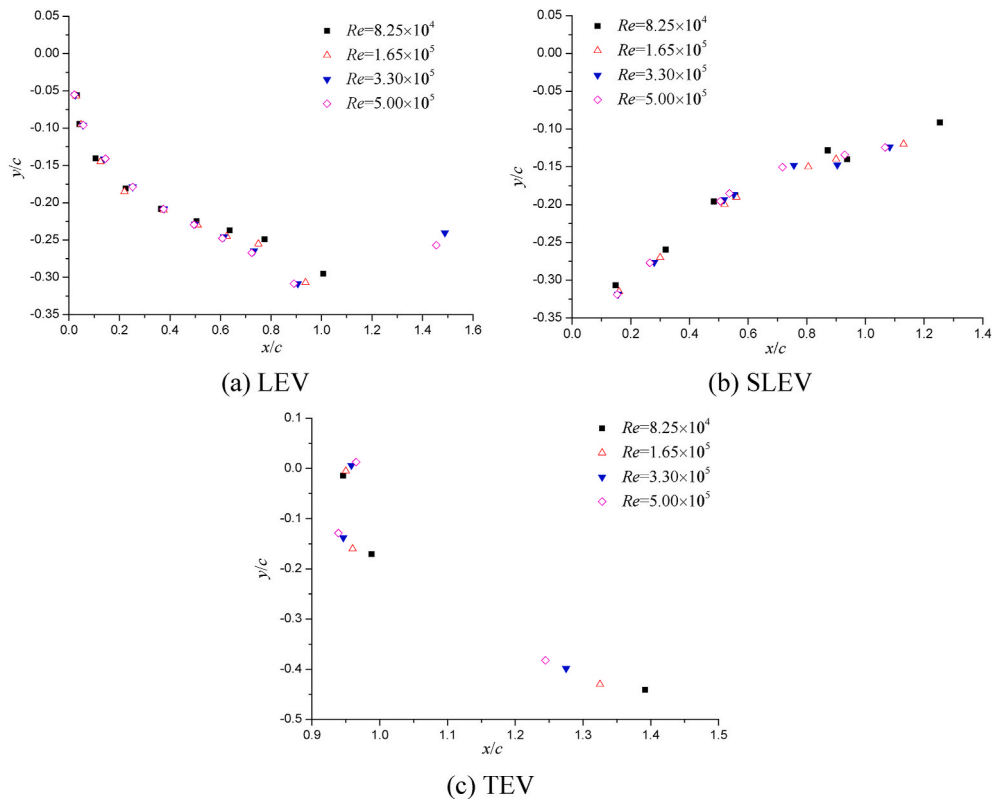
(a) LEV

(b) SLEV

(c) TEV

Fig. 22. Trajectory of different vortices at different *Re*.

necessary to be performed, to get a better prediction of the transition and deep stall flows for the reversed airfoils.

CRediT authorship contribution statement

Lei Shi: Conceptualization, Writing - Original Draft; **Yefang Wang:** Formal analysis, Data curation; **Desheng Zhang:** Supervision, Writing - Review & Editing; **Annie-Claude Bayeul-Lainé:** Supervision, Writing - Review & Editing; **Olivier Coutier-Delgosha:** Supervision, Writing - Review & Editing.

Declaration of competing interest

The authors declare that they have no known competing financial interests or personal relationships that could have appeared to influence the work reported in this paper.

Acknowledgments

References

Almohammadi, K.M., Ingham, D.B., Ma, L., Pourkashanian, M., 2015. Modeling dynamic stall of a straight blade vertical axis wind turbine. J. Fluid Struct. 57, 144–158.

Boutilier, M.S., Yarusevych, S., 2012. Separated shear layer transition over an airfoil at a low Reynolds number. Phys. Fluids 24 (8), 084105 (1-23).

Carrión, M., Steijl, R., Barakos, G.N., Stewart, D., 2016. Analysis of hybrid air vehicles using computational fluid dynamics. J. Aircraft 53 (4), 1001–1012.

Celik, I.B., Ghia, U., Roache, P.J., Freitas, C.J., 2008. Procedure for estimation and reporting of uncertainty due to discretization in CFD applications. J. Fluid Eng. 130 (7), 078001 (1-4).

Chao, L., Pan, G., Zhang, D., 2018. Effect of the asymmetric geometry on the wake structures of a pitching foil. Chin. Phys. B 27 (11), 114701 (1-5).

Dai, H., Luo, H., de Sousa, P.J.F., Doyle, J.F., 2012. Thrust performance of a flexible low-aspect-ratio pitching plate. Phys. Fluids 24 (10), 101903 (1-9).

Ducoin, A., Astolfi, J.A., Deniset, F., Sigrist, J.F., 2009. Computational and experimental investigation of flow over a transient pitching hydrofoil. Eur. J. Mech. B Fluid 28 (6), 728–743.

Granlund, K.O., Ol, M.V., Jones, A.R., 2016. Streamwise oscillation of airfoils into reverse flow. AIAA J. 54 (1), 1628–1636.

Guillaud, N., Balarac, G., Goncalvès, E., 2018. Large Eddy Simulations on a pitching airfoil: analysis of the reduced frequency influence. Comput. Fluids 161, 1–13.

Hodara, J., Lind, A.H., Jones, A.R., Smith, M.J., 2016. Collaborative investigation of the aerodynamic behavior of airfoils in reverse flow. J. Am. Helicopter Soc. 61 (3), 1–15.

Huang, B., Ducoin, A., Young, Y.L., 2013. Physical and numerical investigation of cavitating flows around a pitching hydrofoil. Phys. Fluids 25 (10), 102109 (1-27).

Huebsch, W.W., Rothmayer, A.P., 2002. Effects of surface ice roughness on dynamic stall. J. Aircraft 39 (6), 945–953.

Karbasian, H.R., Kim, K.C., 2016. Numerical investigations on flow structure and behavior of vortices in the dynamic stall of an oscillating pitching hydrofoil. Ocean. Eng. 127, 200–211.

Kim, D.H., Chang, J.W., 2014. Low-Reynolds-number effect on the aerodynamic characteristics of a pitching NACA0012 airfoil. Aero. Sci. Technol. 32 (1), 162–168.

Kim, Y., Xie, Z.T., 2016. Modelling the effect of freestream turbulence on dynamic stall of wind turbine blades. Comput. Fluids 129, 53–66.

Lind, A.H., Jones, A.R., 2015. Vortex shedding from airfoils in reverse flow. AIAA J. 53 (9), 2621–2633.

Lind, A.H., Jones, A.R., 2016a. Unsteady airloads on static airfoils through high angles of attack and in reverse flow. J. Fluid Struct. 63, 259–279.

Lind, A.H., Jones, A.R., 2016b. Unsteady aerodynamics of reverse flow dynamic stall on an oscillating blade section. Phys. Fluids 28 (7), 077102 (1-22).

Lind, A.H., Jarugumilli, T., Benedict, M., Lakshminarayan, V.K., Jones, A.R., Chopra, I., 2014. Flow field studies on a micro-air-vehicle-scale cycloidal rotor in forward flight. Exp. Fluid 55 (12), 1–17.

Lind, A.H., Smith, L.R., Milluzzo, J.I., Jones, A.R., 2016. Reynolds number effects on rotor blade sections in reverse flow. J. Aircraft 53 (5), 1248–1260.

Marchand, J.B., Astolfi, J.A., Bot, P., 2017. Discontinuity of lift on a hydrofoil in reversed flow for tidal turbine Application. Eur. J. Mech. B Fluid 63, 90–99.

Marsh, P., Ranmuthugala, D., Penesis, I., Thomas, G., 2017. The influence of turbulence model and two and three-dimensional domain selection on the simulated performance characteristics of vertical axis tidal turbines. Renew. Energy 105, 106–116.

Martinat, G., Braza, M., Hoarau, Y., Harran, G., 2008. Turbulence modelling of the flow past a pitching NACA0012 airfoil at 10^5 and 10^6 Reynolds numbers. J. Fluid Struct. 24 (8), 1294–1303.

Menter, F.R., Kuntz, M., Langtry, R., 2003. Ten years of industrial experience with the SST turbulence model. Turbulence Heat Mass Transfer. 4 (1), 625–632.

Menter, F.R., Langtry, R.B., Likki, S.R., Suzen, Y.B., Huang, P.G., Völker, S., 2006a. A correlation-based transition model using local variables—part I: model formulation. J. Turbomach. 128, 413–422.

Menter, F.R., Langtry, R., Völker, S., 2006b. Transition modelling for general purpose CFD codes. Flow, Turbul. Combust. 77 (1–4), 277–303.

Nichols, R.H., 2006. Comparison of hybrid turbulence models for a circular cylinder and a cavity. AIAA J. 44 (6), 1207–1219.

Rahromostaqim, M., Posa, A., Balaras, E., 2016. Numerical investigation of the performance of pitching airfoils at high amplitudes. AIAA J. 2221–2232.

Rezaeiha, A., Kalkman, I., Blocken, B., 2017. Effect of pitch angle on power performance and aerodynamics of a vertical axis wind turbine. Appl. Energy 197, 132–150.

Rezaeiha, A., Montazeri, H., Blocken, B., 2019. On the accuracy of turbulence models for CFD simulations of vertical axis wind turbines. Energy 180, 838–857.

Richardson, L., Gaunt, A., 1927. The deferred approach to the limit. Part I. Single lattic. Part ll. Interpenetrationg lattices. The philosophical transcations of the royal society of london. Series A Paper Math. Phy. Character. 116 (3), 405–441.

Roache, P.J., 1994. Perspective: a method for uniform reporting of grid refinement studies. J. Fluid Eng. 116 (3), 405–411.

Roache, P., 1998. Verification and Validation in Computational Science and Engineering. Hermosa Publishers, Albuquerque.

Salari, M., Rava, A., 2017. Numerical investigation of hydrodynamic flow over an AUV moving in the water-surface vicinity considering the laminar-turbulent transition. J. Mar. Sci. Appl. 16 (3), 298–304.

Shen, J.Q., Pan, C., Wang, J.J., Yi, H.M., Li, T., 2015. Reynolds-number dependency of boundary-layer transition location on stratospheric airship model. J. Aircraft 52 (4), 1355–1359.

Singh, K., Páscoa, J.C., 2019. Numerical modeling of stall and poststall events of a single pitching blade of a cycloidal rotor. J. Fluid Eng. 141 (1), 011103 (1-16).

Smith, L.R., Jones, A.R., 2019. Measurements on a yawed rotor blade pitching in reverse flow. Physical Review Fluids 4 (3), 034703 (1-20).

Stern, F., Wilson, R.V., Coleman, H.W., Paterson, E.G., 2001. Comprehensive approach to verification and validation of CFD simulations—part 1: methodology and procedures. J. Fluid Eng. 123 (4), 793–802.

Tseng, C.C., Cheng, Y.E., 2015. Numerical investigations of the vortex interactions for a flow over a pitching foil at different stages. J. Fluid Struct. 58, 291–318.

Tseng, C.C., Hu, H.A., 2016. Flow dynamics of a pitching foil by Eulerian and Lagrangian viewpoints. AIAA J. 54 (2), 712–727.

Visbal, M.R., Garmann, D.J., 2018. Analysis of dynamic stall on a pitching airfoil using high-fidelity large-eddy simulations. AIAA J. 46–63.

Wang, S., Ingham, D.B., Ma, L., Pourkashanian, M., Tao, Z., 2010. Numerical investigations on dynamic stall of low Reynolds number flow around oscillating airfoils. Comput. Fluids 39 (9), 1529–1541.

Wang, S., Ingham, D.B., Ma, L., Pourkashanian, M., Tao, Z., 2012. Turbulence modeling of deep dynamic stall at relatively low Reynolds number. J. Fluid Struct. 33, 191–209.